

Star Formation in Partially Gas-Depleted Spiral Galaxies

James A. Rose, Paul Robertson¹, Jesse Miner, & Lorenza Levy

University of North Carolina at Chapel Hill

Department of Physics and Astronomy, CB 3255, Chapel Hill, NC 27599

jim@physics.unc.edu, paul@astr.as.utexas.edu, jminer@physics.unc.edu,
lorenza.levy@yahoo.com

ABSTRACT

Broadband B and R and H α images have been obtained with the 4.1-m SOAR telescope atop Cerro Pachon, Chile for 29 spiral galaxies in the Pegasus I galaxy cluster and for 18 spirals in non-cluster environments. Pegasus I is a spiral-rich cluster with a low density intracluster medium and a low galaxy velocity dispersion. When combined with neutral hydrogen (HI) data obtained with the Arecibo 305-m radiotelescope, acquired by Levy et al. (2007) and by Springob et al. (2005a), we study the star formation rates in disk galaxies as a function of their HI deficiency. To quantify HI deficiency, we use the usual logarithmic deficiency parameter, DEF . The specific star formation rate (SSFR) is quantified by the logarithmic flux ratio of H α flux to R band flux, and thus roughly characterizes the logarithmic SFR per unit stellar mass. We find a clear correlation between the global SFR per unit stellar mass and DEF , such that the SFR is lower in more HI-deficient galaxies. This correlation appears to extend from the most gas-rich to the most gas-poor galaxies. We also find a correlation between the central SFR per unit mass relative to the global values, in the sense that the more HI-deficient galaxies have a higher *central* SFR per unit mass relative to their *global* SFR values than do gas-rich galaxies. In fact, approximately half of the HI-depleted galaxies have highly elevated SSFRs in their central regions, indicative of a transient evolutionary state. In addition, we find a correlation between gas-depletion and the size of the H α disk (relative to the R band disk); HI-poor galaxies have truncated disks. Moreover, aside from the elevated central SSFR in many gas-poor spirals, the SSFR is otherwise lower in the H α disks of gas-poor galaxies than in gas-rich spirals. Thus both disk truncation *and* lowered SSFR levels within the star-forming part of the disks (aside from the

¹Now at Department of Astronomy, University of Texas at Austin

enhanced nuclear SSFR) correlate with HI deficiency, and both phenomena are found to contribute equally to the global suppression of star formation. We compare our results found in the low richness Pegasus I cluster and in non-cluster environments with SFRs found for HI-deficient spirals in the Virgo cluster by Koopmann & Kenney (2004a,b); Fumagalli & Gavazzi (2008).

Subject headings: galaxies: clusters: general, galaxies: evolution, galaxies: ISM, radio lines: galaxies

1. Introduction

In the cores of nearby galaxy clusters early-type (E/S0) galaxies are the dominant population (e.g., Oemler 1974; Dressler 1980; Gomez et al. 2003; Goto et al. 2003). Furthermore, even the star-forming disk galaxies tend to be depleted in atomic hydrogen (HI), typically by an order of magnitude (e.g., Giovanelli & Haynes 1985; Gavazzi 1987; Solanes et al. 2001; Gavazzi et al. 2006). In contrast, at modest redshifts ($z \gtrsim 0.3$) the fraction of blue, star-forming disk galaxies is substantially higher (Butcher & Oemler 1978, 1984; Dressler & Gunn 1983; Dressler et al. 1999). This rapid recent evolution in the disk galaxy population of clusters provides an excellent opportunity to study the decline of star formation in galaxies, and its causes, and has thus spurred numerous observational and theoretical studies.

The two most prevalent mechanisms for driving disk galaxy evolution in clusters are (1) interaction between the galaxy interstellar medium (ISM) with the diffuse hot intracluster medium (ICM) and (2) gravitational tidal effects. In the first mechanism either ram pressure directly strips the galaxy ISM (Gunn & Gott 1972) via momentum transfer, thermal conduction, and/or viscous stripping removes the ISM through energy transfer (e.g., Nulsen 1982; Cowie & Songaila 1977). In the second mechanism, gas removal is achieved either through major or minor galaxy-galaxy encounters (e.g., Toomre & Toomre 1972; Mihos & Hernquist 1994, 1996), through tidal interaction of the galaxy with the cluster potential (Byrd & Valtonen 1990) or through “harrassment” of a galaxy from numerous impulsive encounters (Moore et al. 1996, 1998). Several cases of asymmetric HI, H α , and radio continuum emission in cluster galaxies have provided detailed and convincing evidence for ram pressure effects (Gavazzi et al. 1995; Kenney et al. 2004; Vollmer et al. 2004; Crowl & Kenney 2006; Chung et al. 2007; Yoshida et al. 2008), and gas dynamical simulations that reproduce the observations in detail are becoming increasingly sophisticated (Abadi et al. 1999; Vollmer et al. 2001; Schulz & Struck 2001; Roediger & Hensler 2005; Kronberger et al. 2008a,b, among others). Nevertheless, tidal interactions are ob-

served to be increasingly common in clusters at higher redshift (e.g., Lavery & Henry 1988; van Dokkum et al. 2000), and thus appear to play an important role as well, especially when galaxies first enter the main cluster in small groups with relatively low velocity dispersion (e.g., van Gorkom 2004; Verheijen 2004). It is in any case clear that ram pressure stripping is more effective on extraplanar and diffuse interstellar gas in galaxies, and tidal interactions indeed produce diffuse extraplanar gas (e.g., Struck & Brown 2004). Hence recent studies tend to advocate a synergy between ram pressure and tidal effects in depleting the ISM in cluster disk galaxies (e.g., Chung et al. 2007; Kapferer et al. 2008). Furthermore, while in principle these mechanisms may completely deplete the ISM of galaxies in the right circumstances, recent studies have tended to support the proposal by Larson, Tinsley, & Caldwell (1980) that “starvation” or “strangulation” of the disk occurs when the (more vulnerable) gas resupply from the outer disk and hot gaseous halo is cut off by the combined effects of ram pressure and tidal interaction (Kawata & Mulchaey 2008). Evidence for gas depletion and altered SFR in cluster spirals, and for the mechanisms driving the observed depletion, is extensively reviewed in Boselli & Gavazzi (2006) and in van Gorkom (2004).

While the fraction of S0 galaxies is highest in the cores of present epoch galaxy clusters, S0s do exist as well in poor clusters and in lower density environments. Given that the balance between ram pressure and tidal effects should vary with environment, an analysis of gas depletion characteristics for galaxies in low density versus rich cluster environments should provide additional constraints on the gas depletion process. The lower velocity dispersions of galaxies in groups should favor tidal interaction over ram pressure effects, when compared to the high velocity dispersion environments of rich clusters. Nevertheless, Hester (2006) has found that partial ram pressure stripping of the less massive spirals should be possible in group environments. In fact, several observational studies have found both individual and statistical evidence for partially HI-depleted galaxies in the group environment. One notable example is the spiral galaxy NGC 2276 in the NGC 2300 galaxy group, which has an asymmetric morphology and high star formation rate indicative of interaction between NGC 2276 and its environment (Davis et al. 1997), is moderately HI deficient by a factor of ~ 2 (Rasmussen, Ponman, & Mulchaey 2006), and is located in the first loose galaxy group for which extended X-ray emission has been discovered (Mulchaey et al. 1993; Rasmussen, Ponman, & Mulchaey 2006). Similarly, HI imaging of spirals in the Holmberg 124 group (Kantharia et al. 2005), Eridanus group (Omar & Dwarakanath 2005), and four X-ray bright groups (Sengupta et al. 2007) find modest HI deficiencies, as well as peculiar HI morphologies indicative of asymmetrical and/or extraplanar gas. Since ram pressure alone appears incapable of clearing out the HI disks to the level observed, Kantharia et al. (2005) and Sengupta & Balasubramanyam (2006) suggest that a combination of tidally assisted ram pressure stripping and evaporation by thermal conduction may be the source of the ob-

served HI deficiencies. In addition, Sengupta & Balasubramanyam (2006) find statistical evidence for a greater HI depletion for galaxies inhabiting X-ray bright groups compared to groups without detected X-ray emission. Evidence has also been presented for HI-depleted galaxies at such large radial distance in the Virgo cluster that the galaxies cannot have yet experienced the central cluster environment (Solanes et al. 2002). However, distance and modeling uncertainties may be sufficiently large that the possibility of these galaxies having passed through the Virgo cluster core remains open (Sanchis et al 2004; Cortes et al 2008). Finally, Springob et al. (2005b) show that the HI mass function in galaxies exhibits some environmental trends, even at local densities that are substantially below the rich cluster level.

A question that naturally arises is whether the HI deficiencies in galaxies translate as well into reduced star formation rates, and if so, how the reduction of star formation is distributed within the disk. As Koopmann & Kenney (2004a,b; hereafter KK04ab), Fumagalli & Gavazzi (2008; hereafter FG08), and others (e.g., Thomas et al 2008) have pointed out, the characteristics of both global SFR in HI-depleted galaxies and the detailed SFR profiles in those galaxies can shed light on the mechanism(s) causing the loss of gas in the high DEF spirals; HI imaging is similarly pertinent (Cayatte et al. 1994; Bravo-Alfaro et al. 2001). A particular emphasis of these previous studies has been to characterize whether the reduced SFR that accompanies HI depletion in Virgo cluster spirals is a result of disk truncation, or whether a more general quenching is occurring of the SFR throughout a normal sized disk. In fact, there is some disagreement between FG08 and KK04ab on this question. KK04ab have carried out a comprehensive investigation of star formation rates in Virgo cluster spirals on the basis of H α and R band imaging. They find relatively few examples of “quenched” galaxies, i.e., with globally lowered SFR in a disk of normal extent. Rather, approximately 50% of the disks in their Virgo spirals are truncated in H α . Furthermore, KK04a find a general correspondence between H α and HI disk sizes and between the morphologies of their H α disks and the HI disk types found by Cayatte et al. (1994). On the other hand, while FG08 do find that the most HI-depleted disks in their Virgo sample are truncated in H α as well, the more modestly depleted HI disks exhibit a more global depression of SFR in an otherwise normal disk size. FG08 thus argue that disk quenching is the key process in Virgo cluster spirals, rather than disk truncation. Clearly, a resolution of the roles of disk truncation versus quenching, in a broad range of environments in addition to the Virgo cluster, would be of considerable importance in assessing what mechanism is chiefly responsible for the removal of atomic gas in galaxy disks.

In a recent study, Levy et al. (2007, hereafter L07) found evidence for mild (factor of 2) HI deficiencies for many spirals in the Pegasus I cluster, which is a low velocity dispersion poor cluster with low X-ray emission. HI imaging of a few of the gas-deficient spirals showed

asymmetries and reduced HI-to-optical disk diameters that further emphasized the anomalous properties of those galaxies. The low ram pressure in Pegasus I, as in the galaxy groups mentioned above, provides an interesting intermediate environment in which to assess the sources of HI deficiencies in disk galaxies.

In this paper, we present optical R band and H α imaging of many of the Pegasus I cluster spirals, as well as other spirals with a variety of HI deficiencies. The goal is to evaluate the connection between star formation properties (i.e., both global and radial star formation profiles) and atomic gas depletion for galaxies in environments outside of rich clusters, with particular emphasis on the Pegasus I galaxy cluster that formed the basis of the L07 study. Our objective is to provide additional constraints on the gas depletion process, with the focus on how such activity occurs in the group environment. In §2 we describe the galaxy samples observed by us, the HI and optical observational data, and the data analysis methods. In §3 we present both the radial star formation profiles and global rates extracted from the H α and R band imaging, and relate them to the data on HI deficiency. Finally, in §4 a discussion of our results is given in the context of other evidence for the sources of HI deficiency in spiral galaxies, and a brief summary is given in §5.

2. Observations

2.1. Samples of Galaxies

Our analysis of the connection between atomic gas depletion and SFRs in galaxies is based on two samples of spiral galaxies. The first is the list of 54 spirals in the Pegasus I galaxy cluster, as well as 17 spirals in a variety of environments approximately 1^{hr} to the East of Pegasus, that formed the basis of the L07 study. Global HI measurements were obtained for all of these galaxies with the Arecibo 305 m radiotelescope for the L07 study. In this paper we supplement those previous 21 cm observations with optical B and R band and H α imaging of 29 of the Pegasus I galaxies and 3 of the galaxies to the East of Pegasus. We refer to this sample of 32 galaxies as the L07 sample. As discussed in L07 the Pegasus I cluster can be divided into three distinct groups, a central group with $3400 \leq cz \leq 4400$ km s $^{-1}$, a foreground group, with $2500 \leq cz < 3400$ km s $^{-1}$, and a background group, with $4400 < cz \leq 6000$ km s $^{-1}$. The background group appears to link up with the Perseus-Pisces Supercluster (Haynes & Giovanelli 1986).

A second sample of spiral galaxies, for which homogeneous global HI data is available from the literature, was observed in B, R, and H α to fill out the optical imaging program when the primary Pegasus I targets were at excessive airmass. We refer to this second

sample of 15 galaxies as the supplementary sample. Specifically, we selected non-cluster Sa-Sc galaxies from the Springob et al. (2005a, hereafter S05a) catalog for which Arecibo observations have been made, and covering a variety of HI deficiencies (The nature of the S05a catalog is further discussed in §2.2). We also restricted the sample to the redshift range $2700 < cz < 5500 \text{ km s}^{-1}$, which corresponds to the useful range of the 100 Å wide H α interference filter used for the observations. Furthermore, we intentionally selected galaxies covering a range in neutral hydrogen deficiency (HI deficiency is defined in the next Section). Hence our supplementary sample is far more biased towards galaxies with larger HI deficiency than a random selection from the S05a catalog would produce.

A key parameter for the galaxies in this supplementary sample (as well as for the galaxies in the L07 sample) is the local environment in which the galaxy is located. While different techniques have been applied to define local environment, including projected galaxy surface density on the sky, we have chosen to use a three-dimensional number density in which the position of each galaxy is calculated from its sky position and recessional velocity. To construct a density field, we used the Updated Zwicky Catalog of Falco et al. (1999, hereafter UZC), which is 95% complete to a limiting magnitude of $m_{Zw} = 15.5 \text{ mag}$, includes galaxies of all types, and covers most of the northern sky. Using the sky positions and local-group-corrected redshifts of the objects in the UZC, and adopting a value of the Hubble constant of $H_0 = 75 \text{ km s}^{-1}$, we assign each galaxy a 3D position in a Cartesian coordinate system. To calculate the local density, we find the mean distance to an object’s six nearest neighbors, and use that distance to define the radius of a sphere containing the “local” region. The number of objects contained within the sphere is divided by the physical volume of the sphere to obtain a number density in units of Mpc^{-3} . This number density is then corrected for the (in)completeness of the galaxy luminosity function, relative to the degree of completeness at $cz = 3000 \text{ km s}^{-1}$. Specifically, we have multiplied all of the calculated densities by a LF correction factor which is the ratio of the integrated observable LF (i.e., the number of galaxies per Mpc^3 brighter than the limiting magnitude of the sample) at 3000 km s^{-1} to the integrated LF at the galaxy’s redshift. We use a Schechter LF (Schechter 1976) derived from the UZC, with $\alpha = -1.0$ and $M_B^* = -18.8$ (Marzke et al 1994).

In summary, our dataset is based on two samples. The first, L07, sample consists of Arecibo HI data and optical B, R, and H α imaging for 29 galaxies in the Pegasus I cluster and 3 non-cluster galaxies to the east of Pegasus. The second, supplementary, sample consists of 15 target of opportunity non-cluster galaxies for which Arecibo data, compiled in a homogeneous manner in the S05a catalog, also exists. Our combined sample is distinct from those of KK04ab and FG08 in that both of the latter samples are entirely based on the Virgo cluster environment. In contrast, our galaxies span a range of lower density environments, with greatest emphasis on the spiral-rich low velocity dispersion Pegasus I cluster. The range

in luminosity of our galaxies is quite similar to that in KK04ab, while the luminous Virgo spirals studied in FG08 are typically 1-1.5 mag more luminous than our spirals.

Coordinates (equinox 2000.0) for our galaxy sample, as well as morphological types, redshift information, and the above-described local number density are listed in Table 1. The morphological T type, given in column (5), and the heliocentric redshift, in column (6), are taken from HyperLeda. The Log Density (in galaxies per Mpc^3) is given in column (7). A description of the HI and optical data is given below.

2.2. HI Data

Global HI measurements of 54 spiral galaxies in the Pegasus I cluster, as well as for 17 spirals approximately 1^{hr} east of Pegasus, were obtained with the Arecibo 305 m telescope by L07. Details on the observations are given in that paper. Here we concentrate on the HI data for the 29 Pegasus I spirals and 3 non-Pegasus spirals for which we have newly acquired broadband optical and $\text{H}\alpha$ imaging.

Neutral hydrogen data for the 15 spirals in our second sample are taken from the S05a catalog, which consists of global HI fluxes for over 8,000 spiral galaxies observed with several radio telescopes over a span of some 20 years. The flux measurements have been re-processed to correct for instrumental effects such as beam attenuation and pointing offsets, as well as HI self-absorption in the observed galaxies. Thus, the corrected fluxes can be assumed to be homogeneous. While the catalog also includes data from other radio telescopes, we have only used Arecibo observations to avoid any instrument-to-instrument offsets.

For both the L07 galaxies and the supplementary 15 galaxies from the S05a catalog the global 21 cm flux is used to calculate the total HI mass of each galaxy. Specifically, $M_{HI} = 2.36 \times 10^5 (hr)^2 F_{HI} M_{\odot}$, where r is the radial distance in kpc and F_{HI} is the corrected 21 cm flux density in Jy km s^{-1} (Solanes et al. 1996). The linear optical diameter is given by $D_0 = 0.291(hr)a$ kpc, where a , the angular major axis diameter, is also provided by the S05a catalog.

2.2.1. Determination of HI Deficiency

The focus of this paper is to investigate the relationship between neutral hydrogen depletion in galaxy disks and the global and local star formation rates. To quantify the degree to which a particular galaxy is deficient in HI we must compare the observed HI content with the amount of HI that is *expected* in a galaxy of its morphological type and

size. The logarithmic difference between the expected and observed gas content will then represent the gas deficiency of the galaxy (DEF). Here we describe how the expected HI content is determined for the various galaxies in the L07 sample and in the supplementary sample of galaxies extracted from the S05a catalog.

L07 calculate DEF values for the galaxies in the Pegasus region using the prescription detailed in Solanes et al. (1996), as follows. First, we recall that there is a logarithmic correlation between a galaxy’s HI mass and its linear diameter, with a slight dependence of the slope of the fit on morphological type. If a fit of $\log(M_{HI})$ vs. $\log(D_0)$ is performed on a sample of normal galaxies of the same morphological type, then the best fit line is taken to represent the expected HI mass as a function of linear diameter. At a given diameter, if the measured HI mass is less than that predicted by the fit to the sample, then the galaxy is defined to have a positive deficiency (DEF), given by the logarithmic difference between the expected and the observed values:

$$DEF = (\log M_{HI}(D_0, T))_{exp} - \log M_{HI}, \quad (1)$$

Before one can perform these fits, however, a suitable sample of galaxies must be chosen to represent a “normal” population in terms of HI content. Due to the increased likelihood of a galaxy to be gas deficient with increasing local density, this sample must be restricted to low density environments to base the deficiency measurement on galaxies whose gas content is dictated primarily by the fluctuations of secular evolution, not environmental effects. Solanes et al. (1996) use a survey of 4620 galaxies from the Perseus-Pisces supercluster region, and define a low density sample of 2582 galaxies based on the sky-projected surface density of galaxies. All of the galaxies in low surface density regions are combined according to morphological type and used to perform the $\log(M_{HI})$ - $\log(D_0)$ fit. A large galaxy sample is necessary due to the existence of a natural scatter around the mean $\log(M_{HI})$ - $\log(D_0)$ relation. The slopes and zero-points from these fits are then used to determine the expected HI content for all of the galaxies in the sample. The DEF values of L07 come directly from these results.

For the 15 galaxies in the supplementary sample we have used 21 cm flux measurements from S05a, as previously mentioned. Unlike L07, we have elected to define the “normal” galaxy population for HI content in a manner that is more consistent with our own local density measurements.¹ The DEF values for these 15 galaxies are based on $\log(M_{HI})$ - $\log(D_0)$ fits for a large galaxy sample drawn from the whole Springob et al. (2005a) catalog, which

¹We are carrying forward this redefinition of “normal” HI content to work in progress on the relation between HI deficiency and environment. Hence we wish to establish consistency in this paper with the future study.

the criterion that local galaxy densities be less than $-1.0 \log \text{Mpc}^{-3}$ (as described in section 2.1). We have also chosen a velocity range of $3,000 \text{ km s}^{-1}$ to $6,500 \text{ km s}^{-1}$ for selecting a low-density galaxy sample. The lower limit is applied to prevent peculiar velocities from dominating the observed redshift and affecting the line-of-sight distance measurements (and, more specifically, to avoid the Virgo supercluster). We apply an upper velocity limit of $6,500 \text{ km s}^{-1}$ due to the rapidly increasing uncertainty in the LF correction to the observed local density (discussed in the previous Section), which occurs as the observable LF becomes restricted to only the bright end at higher redshift. Of the original $>8,000$ galaxies in the S05a sample, about 3,000 galaxies meet the density and velocity criteria, which provides a large enough sample to span the necessary morphological types for fitting the $\log(M_{HI})$ - $\log(D_0)$ relation. We then perform the same steps described above for calculating the DEF parameter on the S05a galaxies, where the expected HI mass is now given by the fits performed on our low density sample.

It is important to verify that the HI flux and DEF data in L07 is consistently on the same scale as the HI flux data for the 15 galaxies in the supplementary sample extracted from HI flux data in S05a, and for which we produced a different definition of “normal” HI content. To do so, we have extracted HI flux data for all galaxies in common between L07 and S05a. For those 25 galaxies we have compared the DEF values given in L07, which are based on their own Arecibo HI data and on the Solanes et al. (1996) prescription for “normal” HI content, with the DEF values calculated from the S05a HI data and with the “normal” HI content determined from our new fits to the $\log(M_{HI})$ - $\log(D_0)$ relation. As seen in Fig. 1, the agreement between the two data sources is good. The thick dashed line shows the linear least squares fit between the two DEF values for all 25 galaxies in common between L07 and S05a, while the thick solid line indicates the fit achieved when the single most discrepant galaxy, NGC 41, is excluded. The slope of the fit is 0.96 ± 0.08 and 0.99 ± 0.06 with and without including NGC 41; the rms scatter about the linear fit is ± 0.15 and ± 0.12 respectively. We cannot account for the discrepancy in DEF between the two sources in the case of NGC 41, since the HI fluxes only differ by 16% and the morphological types assumed are the same. We attribute the difference to a calculation error in L07. In the case of the next most discrepant galaxy, UGC164, the larger DEF value given in L07 is attributable to the 50% lower HI flux reported by them. To maintain consistency with the previous work, we continue to use the L07 HI flux and DEF data for the galaxies in that paper, with the exception of NGC 41, for which we adopt the flux data from S05a and DEF calculation based on the “normal” HI content derived for this paper. Data on DEF for the galaxies in our combined sample is given in column (2) of Table 2.

To illustrate the range of DEF and $\log(\rho)$ covered by our Pegasus I and non-cluster samples, we have plotted DEF versus $\log(\rho)$ in Fig. 2. The Pegasus I galaxies, plotted as

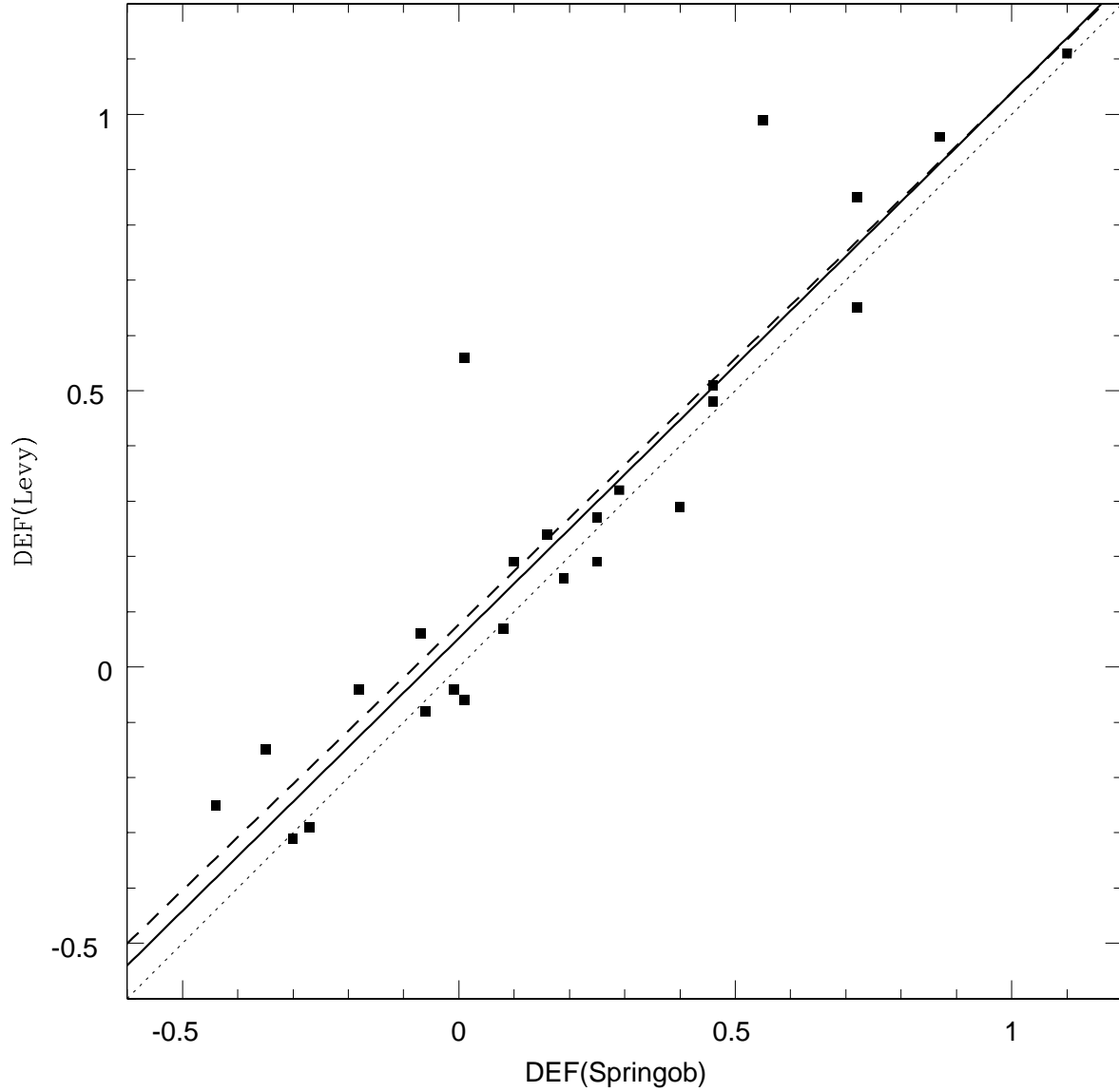


Fig. 1.— The HI deficiency DEF parameter given in L07 (vertical axis) is compared with that determined for this paper from HI flux data in S05a and our revised prescription for “normal” HI content (horizontal axis). The thin dotted line denotes the unit slope line, while the thick dashed line shows the fit to all 25 galaxies in common between the two samples, and the thick solid line shows the fit when the most discrepant point is excluded.

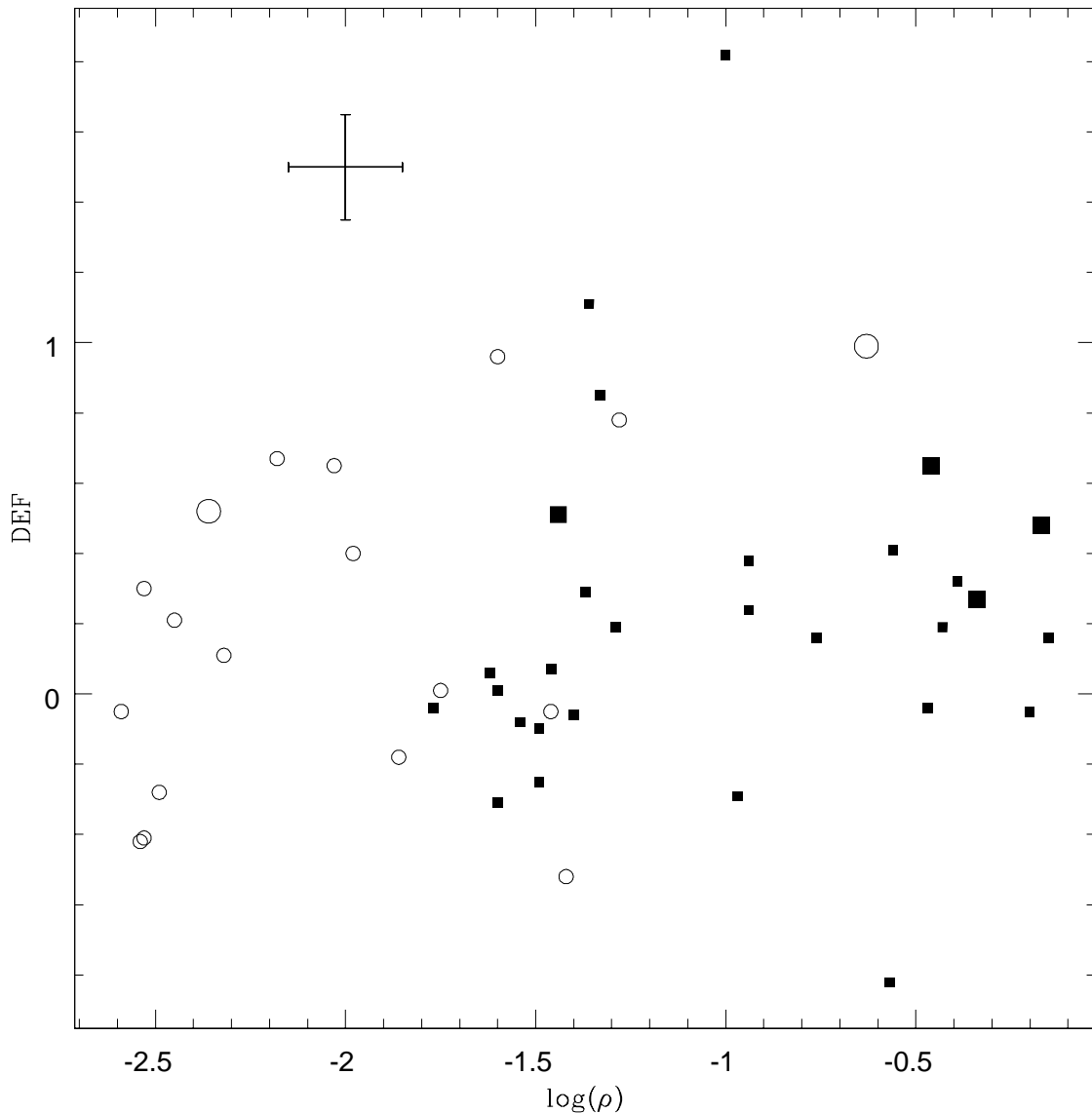


Fig. 2.— The HI DEF parameter (defined in §2.2) is plotted versus $\log(\rho)$, the local environmental density in $\log \text{Mpc}^{-3}$ for the data in our combined sample. Filled squares denote Pegasus I cluster spirals and open circles are for the non-cluster spirals. The larger filled squares and open circles denote cluster and non-cluster galaxies, respectively, which have both high DEF and high central SSFR (i.e., high $\gamma(0.1)$), as discussed in §3.2. Note that the non-cluster spirals were preferentially selected to cover a range in DEF at different environments, hence this figure demonstrates the range of environment and DEF in the sample, but not a relationship between the two.

filled squares, on the whole cover a higher local density regime than the non-cluster galaxies, plotted as open circles.

2.3. Optical Imaging

Broadband B and R and narrowband H α (both online and offline) images were obtained for 29 galaxies in the Pegasus I cluster and for 18 additional spiral galaxies with Arecibo HI data with the 4.1-m SOAR telescope atop Cerro Pachon in Chile during the time period August 2006 through August 2008. All images were acquired with the SOAR Optical Imager (SOI). SOI is a focal reducing camera mounted at a bent Cassegrain port on SOAR, with a scale of 0.154"/pixel when read out in 2x2 binned mode (Schwarz et al. 2004). The 5.3' field of view is covered by two E2V 2Kx4K CCDs, with a 7.8" gap between them. The gain is 2.1 e⁻/ADU and the read noise in binned mode is $\sim 4.5e^-$. In almost every case the galaxy was small enough to fit on a single chip, thereby avoiding the added complexity of stitching together multiple dithered exposures to remove the effect of the interchip gap.

The broadband B and R filters are the standard SOI filters, while the H α online and offline filters were fabricated by Custom Scientific, Inc. in Phoenix, AZ. The online filter is centered at 6660 Å, corresponding to a redshift of ~ 3700 Å in the f/9 converging beam, while the offline filter is centered at 6840 Å. Both filters have a FWHM of 100 Å.

For both the broadband B and R filters a series of three 150 second exposures was acquired. For the H α online and offline filters, three 300 second exposures were taken for each galaxy. On a typical night 4-6 standard star fields from Landolt (1992) were observed, with typically 3-4 stars observed per field.

2.3.1. Image Analysis

All images were analyzed with the NOAO/IRAF 'mscred' package. Each raw image consisted of four image extensions, given that there are two amplifiers on each CCD chip, and two chips in the SOI instrument. First, the overscan on each amplifier was fit with a linear polynomial and removed, and the data frame was slightly trimmed. Next, a master bias frame, combined from a median of typically 25 frames, was subtracted from all object and calibration images. Flat fielding was accomplished by creating a master flat from typically six sky flat images, taken during evening and/or morning twilight, and with exposure times adjusted to reach a count level at approximately half of the linear range of the detector. The flats were median-combined in the 'flatcombine' task, with rejection of minimum and

maximum values. Dome flats were taken as well in each filter every afternoon. In practice we found that dome flats and sky flats produced virtually identical results in the R bandpass, and in the H α online and offline filters, i.e., at red wavelengths. For the broadband B filter, there were significant differences between dome and sky flats, due to the plunging spectral energy distribution of the dome flats in the blue. Hence sky flats in B were seen to make a far better match to the object frames, in terms of dividing out obvious structure in the raw images in scales of tens of pixels. We consequently used sky flats for all of our flat fielding. Dividing through by the sky flat can be problematic if there is a significant field distortion over the full field of view of the image. However, in the case of SOI the maximum scale variation from center to edge of field is only $\sim 0.15\%$ at red wavelengths.

At this point the image consisted of four extensions that had been individually treated. The next step was to combine the four amplifiers into a single mosaic image, using an IRAF script written by Dr. Alexandre Oliveira. Finally, to combine the three individual exposures in each filter into a single frame required first registering the images, and then combining them with cosmic ray rejection. The tasks ‘mscmatch’ and ‘wregister’ were used in the ‘mscred’ package to register the images. The ‘combine’ task, with median scaling and averaging with the ‘crreject’ cosmic ray rejection option, were used to combine the three frames into the final image.

Since the image quality can differ between the final R band and H α online and offline images, the full width half maximum was determined for each bandpass from several stars in the field. Then all images were gaussian convolved to the same FWHM as the worst seeing bandpass.

2.3.2. Sky Removal and Profile Fitting

Accuracy of background subtraction typically is the limiting factor in pursuing galaxy surface photometry at low surface brightness levels. We found that even after bias subtraction and flat-field division there is often a residual discontinuity in the background level across amplifiers on a chip, and across the boundary between chips. The discontinuities could be as large as one ADU per pixel in the broadband R images, out of a background of approximately 200 ADU, and were usually not constant throughout the night. Thus to keep our background subtraction accurate to the 10% level, we limited the surface photometry in the R bandpass to a minimum count level of 10 counts/pixel. Based on the standard star data for the photometric nights, a level of 10 cts/pix corresponds to a surface brightness of ~ 24.75 mag arcsec $^{-2}$ in R at the typical airmass of our observations. This surface brightness zero point is consistent with ‘Lick r’ band surface photometry given in Courteau (1996)

for 5 galaxies in common with our sample. For those 5 galaxies the radius that we find at the $R=24.75$ mag arcsec⁻² isophote is on average 7% smaller than the $r=25$ mag arcsec⁻² isophotal radii determined by Courteau (1996). We similarly restricted the $H\alpha$ photometry to count levels brighter than 0.5 cts/pix in the online and offline filters.

Sky background was found from the median count levels in regions on the same chip as the galaxy that were found to be free of bright objects. These regions were defined interactively on the image and the mean value for the multiple regions was used as the final background level.

Once the sky background was removed from the $H\alpha$ online and offline images, aperture photometry was performed on several stars. The offline image was normalized to attain the same mean stellar counts as in the online image. The final $H\alpha$ image is the difference between the online and normalized offline images.

For almost all of the finalized R band images, we used the ‘ellipse’ task in the ‘stdas/isophote’ IRAF package to determine an azimuthally averaged radial R band profile for each galaxy. The ‘ellipse’ task starts with initial approximations to the x-y center, position angle, and ellipticity of the isophote at a specified radial distance, then, iterates to optimum values, then steps along to both larger and smaller radii. Among the results tabulated at each azimuthally averaged radius are the surface brightness level, in counts/pix and in magnitudes, the total magnitude within the radius, and errors on all quantities. As mentioned above, we cut off our analysis at a surface brightness level of 10 cts/pix, corresponding to a surface brightness in R of ~ 24.75 mag/sq. arcsec. In a few cases the galaxy was either so close to edge-on, or so irregular in morphology, that profile fitting could not be accomplished reliably. For those galaxies we instead used the ‘polyphot’ task to interactively draw a polygonal boundary around the galaxy, within which the total magnitude was integrated. Thus in these cases only a total R magnitude was determined, as opposed to radial profiles. With a little experimentation using both ‘polyphot’ and ‘ellipse’ tasks, we found that by eye a polygon could readily be drawn around a galaxy which returned the same global magnitude as produced from ‘ellipse’ at the 10 cts/pix isophote.

The $H\alpha$ image is naturally less subject to stable isophote fitting than the R band image. Consequently, for each galaxy we applied the x-y center, PA, and ellipticity information determined from the R band profile fitting to the $H\alpha$ image. In the case of those galaxies for which only global R band magnitudes were attained with ‘polyphot’, the same polygon was applied to the $H\alpha$ image. However, there were a few galaxies with just a few low luminosity HII regions. For those cases we carried out aperture photometry of the individual HII regions, and then calculated a combined $H\alpha$ flux. The $H\alpha$ flux includes as well the emission in the neighboring [NII] $\lambda 6548, 6584$ forbidden lines.

2.3.3. Measurement of Specific Star Formation Rates

From the above analysis we extracted the following information. First, we define the parameter Γ , a global characterization of the star formation rate per unit stellar mass, by taking the base 10 logarithm of the total H α flux within the 0.5 cts/pix isophote divided by the total R band flux within the 10 cts/pix isophote, as follows:

$$\Gamma = \log \left(\frac{f_{H\alpha}}{f_R} \right) \quad (2)$$

The Γ parameter is essentially equivalent to the “normalized massive star formation rate” discussed in KK04ab. The H α flux characterizes the current star formation rate (SFR) of massive stars, while the R band flux is a rough characterization of the total stellar mass, assuming that the mass to R band light ratio is roughly constant in our disk galaxy sample. Since both the H α and R band data were acquired within a short enough time period that the airmass of the galaxy did not change substantially, and since the R band and H α filters are at similar wavelengths, the raw flux ratio did not require correction for extinction effects. We henceforth refer to this normalized SFR as the *specific* star formation rate, or SSFR. Note that our version of the SSFR is slightly different than that used by other authors because we are not basing it on flux-calibrated H α and R band photometry. Thus the zeropoint of our SSFR values will differ from that of other investigators, but the relative values should be on the same scale.

As pointed out by FG08, there is a systematic luminosity dependence in the SFR per H band luminosity, i.e., more luminous galaxies have a lower SSFR. FG08 found a slope to that relation of -0.26 in the log of the SFR per unit H band luminosity versus the log of the H band luminosity, with a substantial (~ 0.3 mag) scatter. To account for this trend in our analysis, we have applied the FG08 correction as follows. We calculated the M_H for all galaxies in our sample using the total H band magnitude and distance modulus given by Hyperleda. In cases where Hyperleda provides only the total B magnitude, we assumed an average $B - H$ color of 2.52, determined from the mean of our sample for which data on both passbands is available. We then defined a corrected version of the log of the H α to R band flux, Γ^* , given by:

$$\Gamma^* = \Gamma + 0.26[-0.4(M_H + 22.50)], \quad (3)$$

where the correction is defined to be zero for an absolute H magnitude of -22.50, which is the mean for our sample. Data on Γ , Γ^* , and M_H are given in columns (3), (4), and (5) of Table 2. The radius, in arcseconds, containing the azimuthally averaged surface brightness

level 10 counts/pixel, r_{10} , is given in column (6) of Table 2. The ratio of the $H\alpha$ radius (i.e., to the 0.5 cts/pix level) to r_{10} , $r_{H\alpha}/r_{10}$, is listed in column (7). The half-light effective radius, r_{eff} , which is determined from the surface brightness profile, is given in column (8).

Errors in the Γ and Γ^* values are difficult to assess, given that the photon statistical errors are exceedingly small, thus systematic errors dominate. We have identified two primary sources of systematic uncertainty, namely, (1) uncertainties in establishing the mean sky level and (2) uncertainties in fitting non-axisymmetric disk structure with ellipses and low order deviations. We evaluated the first uncertainty by experimenting with different sky levels, and the second with comparing isophotal fit fluxes with those extracted from subjectively defined enclosed polygons (using the IRAF 'polyphot') task. We estimate the $\pm 1\sigma$ errors in Γ and Γ^* (and in the later defined $\Gamma_{H\alpha}$, Δ , and $\gamma(0.1)$ quantities) to be $\sim \pm 0.15$ mag. The errors are larger for the lower surface brightness galaxies with faint and irregular HII regions. We estimate the $\pm 1\sigma$ errors in $r_{H\alpha}/r_{10}$ to be typically $\sim \pm 0.2$. The error in DEF is estimated to be $\sim \pm 0.15$.

In addition to the global SSFR, we produced the radial profile of the log of the $H\alpha$ to R band flux ratio from the azimuthally averaged ellipse fitting. We refer to this radially dependent quantity as $\gamma(r)$. In Fig. 3 radial profiles are illustrated for both an HI-depleted galaxy (NGC7518) in the left panel and an HI-rich galaxy (UGC11524) in the right panel. The differences in the radial profiles of the two galaxies is discussed later. In Fig. 4 R band and $H\alpha$ images are shown for both galaxies.

2.4. Optical Spectroscopy

Optical spectra of three HI-deficient galaxies were obtained with the Goodman Spectrograph at the SOAR telescope on the night of September 14-25, 2008. These three galaxies are examples of HI-deficient spirals with high central SSFR that are defined and discussed in §3.2. The Goodman Spectrograph is an all-refracting optics imaging spectrograph mounted at one of the Nasmyth foci, and utilizes volume phase holographic gratings as the dispersing element (Clemens et al. 2004). The spectra are imaged onto a 4k x 4k Fairchild 486 back-illuminated CCD. For our observations the spectra were binned by 2 pixels in the dispersion direction and by 4 pixels along the slit. With the 600 lines/mm VPH grating the binned pixels sample the spectrum at 1.3 Å/pix, at a resolution of 7 Å FWHM, and cover the spectral range 4350-7000 Å. A 1.65" x 3.9' slit was used at the North-South position angle for all observations. Wavelength calibration was achieved with a HgCuAr lamp. For each galaxy a pair of 300 second exposures was acquired.

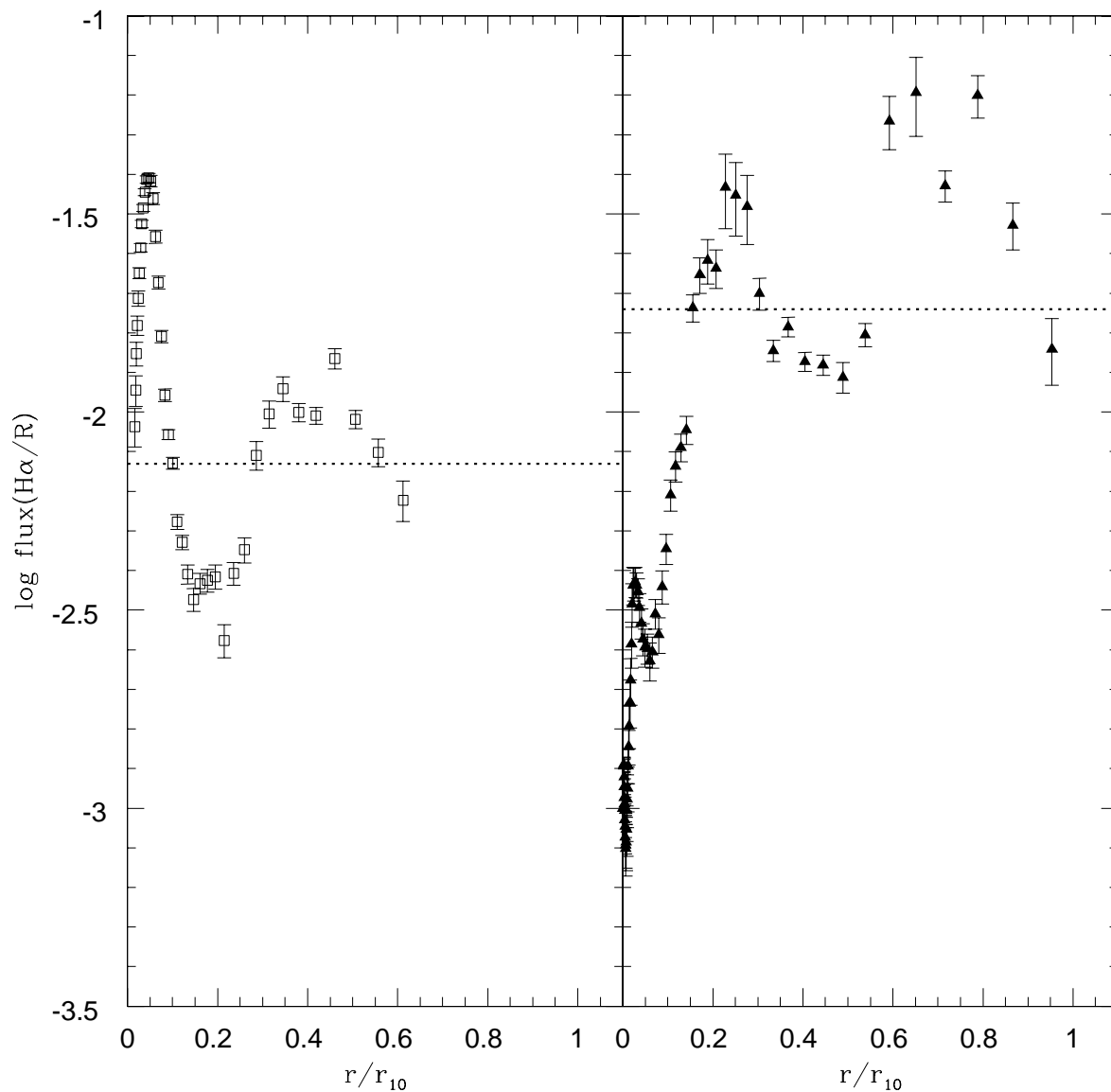


Fig. 3.— Azimuthally averaged radial profiles for the logarithm of the flux ratio in $H\alpha$ to that in the R bandpass are plotted against normalized radial distance. The radial distance is normalized by the radius of the 10 cts/pix isophote. The galaxy in the left panel, NGC7518, is HI deficient, with $DEF=0.27$, while the galaxy in the right panel, UGC11524, is HI-rich, with $DEF=-0.52$. The error bars correspond to the 1σ errors in both the R and $H\alpha$ fluxes, combined in quadrature. The horizontal dashed line in each panel represents the global value of the $H\alpha$ to R band flux ratio for that galaxy.

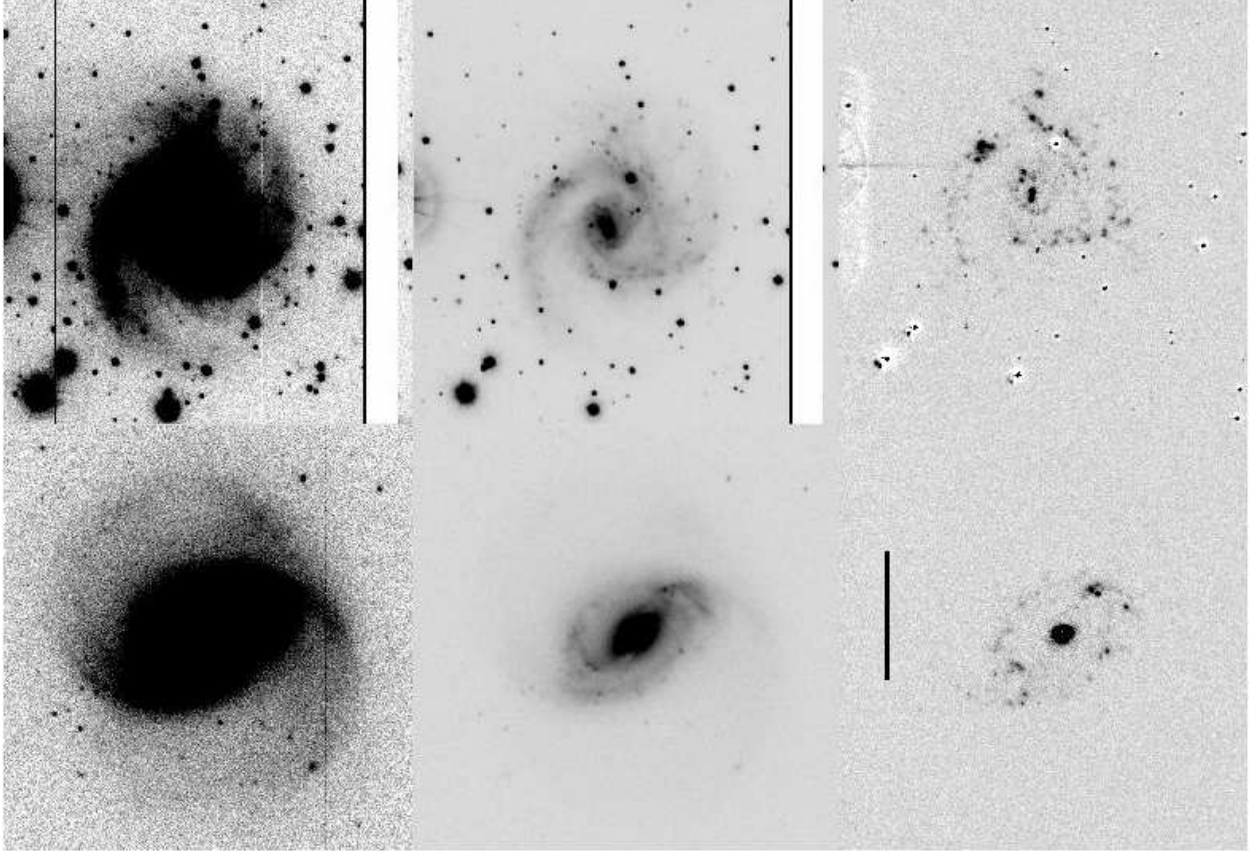


Fig. 4.— R band and $H\alpha$ images are displayed for the gas-rich spiral UGC11524 (upper panels) and for the gas-depleted spiral NGC 7518 (lower panels). The R band images are shown at two contrast levels in the left and middle panels, while the $H\alpha$ images are shown in the right panels. The black line in the lower right panel indicates an angular scale of $30''$.

3. Results

The primary goal of this paper is to investigate whether HI deficiency in spiral galaxies is also reflected in star formation rates. Specifically, we first investigate whether a global HI deficiency in a spiral disk produces a corresponding global suppression in SSFR. We then examine our radial SSFR profiles to assess whether galaxies with global HI deficiencies exhibit characteristic signatures in the radial distribution in SSFR, for instance, truncation of the star forming disk.

3.1. Global SFR

To assess whether a global deficit in atomic hydrogen in spirals is connected with the global SSFR, in Fig. 5 we have plotted the SSFR parameter, Γ^* , versus the HI DEF parameter. The large filled circle denotes the lower limit in DEF and upper limit in Γ^* for NGC 7563. As previously discussed, Γ^* is a measure of the SSFR, corrected for the correlation between SSFR and total H band luminosity. As seen in Fig. 5, there is a trend toward lower SSFR with increasing HI deficit. A linear least squares fit between Γ^* and DEF, which does not include NGC 7563, yields a correlation coefficient $r=-0.68$, with rms scatter of 0.46; the probability that the two variables are uncorrelated is rejected at the 2×10^{-7} level. Thus Γ^* and DEF are clearly related. The linear fit is denoted by the solid line in Fig. 5, and is plotted only over the DEF range for which it is constrained. We have also plotted the quadratic fit (dotted line), which yields an rms scatter of 0.45. The slope of the linear fit is -1.05 ± 0.17 . Replacing Γ^* with the “uncorrected” $\Gamma = \log \frac{f_{H\alpha}}{f_R}$ produces virtually identical results. As previously mentioned, FG08 found a substantial intrinsic scatter in their relationship between SSFR and L_H , thus a considerable intrinsic scatter is present in the global SSFR of galaxies, in addition to any dependence on DEF or environment.

While the quadratic fit indicates a flattening of the relation between Γ^* and DEF at lower DEF, i.e., for gas-rich galaxies, it does not significantly lower the rms residual. Hence, it would appear as if a linear fit is sufficient to describe the relation, with the implication that the global SSFR tracks the global HI even into the gas-rich regime. However, a closer look at Fig. 5 indicates that the scatter around both linear and quadratic fits is dominated by the large intrinsic scatter at high DEF, and thus cannot be improved by increasing the order of the fit. We consequently divided the sample into high ($DEF \geq 0.0$) and low ($DEF < 0.0$) galaxies. We made separate linear least squares fits to the two samples, which yields a slope of -1.22 ± 0.31 and rms residual of ± 0.52 for the 30 high DEF galaxies, and a correlation coefficient of $r=-0.60$. The hypothesis that there is no correlation between Γ^* and DEF in the high DEF sample is rejected at the 0.00048 level. For the 17 galaxies in

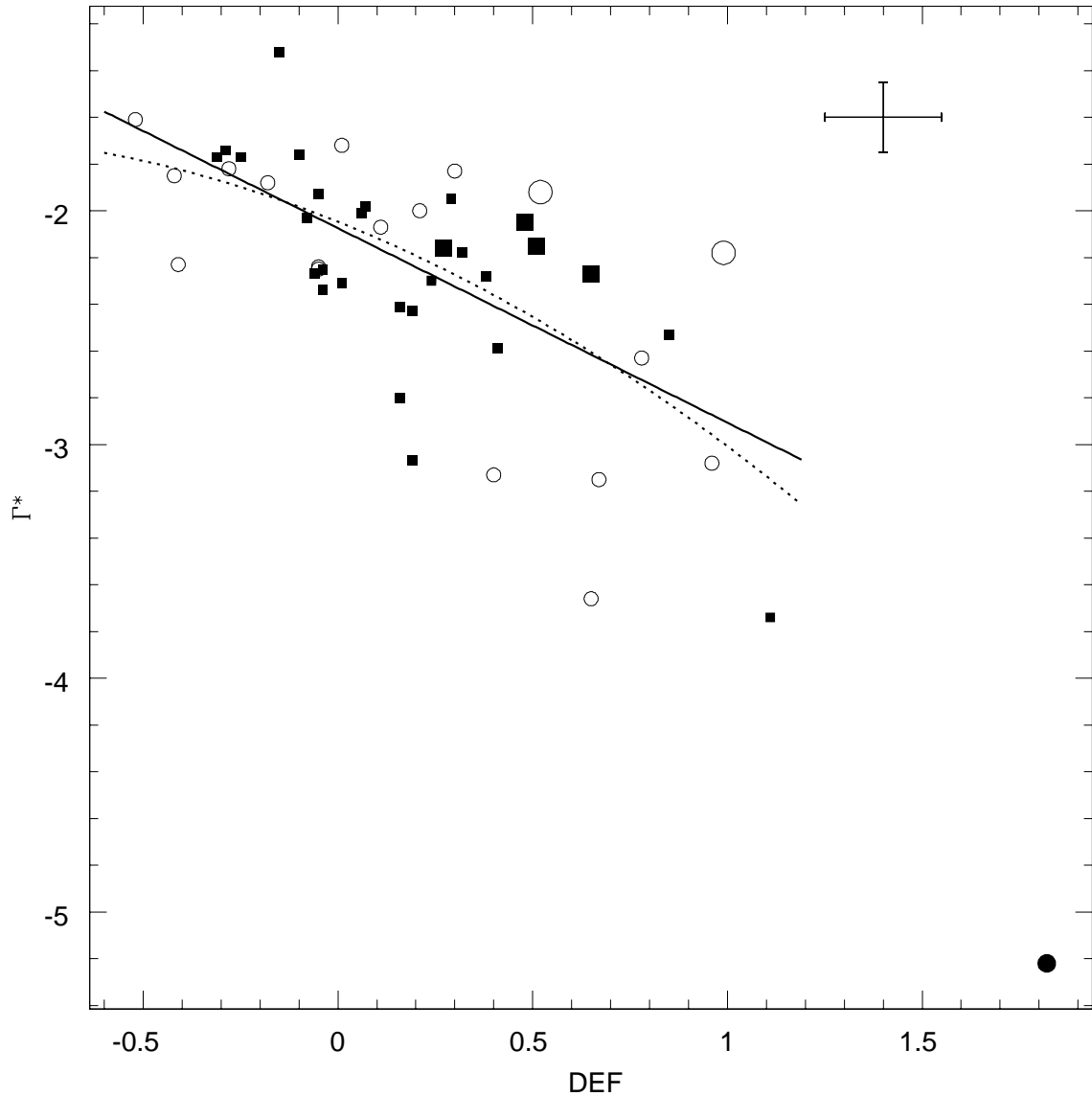


Fig. 5.— The corrected global SSFR parameter, Γ^* (defined in §2.3.3), is plotted versus the gas deficiency parameter, DEF, for the data in our combined sample. Filled squares denote Pegasus I cluster spirals and open circles are for the non-cluster spirals. The larger filled squares and open circles denote cluster and non-cluster galaxies, respectively, which have both high DEF and high central SSFR (i.e., high $\gamma(0.1)$), as discussed in §3.2. The linear least squares fit is shown as a solid line, while the quadratic fit is shown as the dotted curve. The large filled circle represents an upper limit in Γ^* and a lower limit in DEF for the galaxy NGC 7563, and is not included in the fits. The error bar in the upper right corner shows typical $\pm 1\sigma$ errors.

the low DEF sample, we obtain a slope of -0.79 ± 0.57 and rms residual of ± 0.33 . With a correlation coefficient of $r = -0.34$ the hypothesis of no correlation is only rejected at the 0.18 level. However, if the one discrepant galaxy with $\Gamma^* > -1$ is excluded, we then obtain a slope of -0.92 ± 0.32 and rms scatter of only ± 0.18 . The correlation coefficient is $r = -0.61$, and the no correlation hypothesis is rejected at the 0.011 level.

To summarize, there is a clear correlation between Γ^* and DEF, with SSFR decreasing with increasing HI deficiency. This result confirms that found for Virgo spirals in KK04ab and FG08. If the one very high Γ^* galaxy at low DEF (i.e., gas-rich) is excluded, then the trend between Γ^* and DEF is significant at greater than the 3σ level at both high ($\text{DEF} \geq 0.0$) and low ($\text{DEF} < 0.0$) DEF. While the slope derived for low DEF galaxies is formally lower than for high DEF galaxies, the difference is not statistically significant. Hence our main conclusion is that the relation between Γ^* and DEF extends from gas-rich to gas-poor spirals. We also find that the rms scatter around the relation is substantially higher for the high DEF (gas-poor) galaxies.

3.2. SFR Profiles

We now consider whether in high DEF galaxies the SSFR is suppressed throughout the galaxy, or whether it is preferentially lower (or higher) at particular locations in the disk. As is discussed in §4, this question has been addressed by KK04ab and FG08 for Virgo cluster spirals, with some disagreement between the two studies. Given that conclusions regarding the relative importance of starvation versus stripping phenomena can be arrived at from the characteristic depletion patterns in both SSFR and HI, the detailed radial profiles in $\gamma(r)$ are worth a careful examination.

To begin with we return to Fig. 3, in which the radial profiles in $\gamma(r)$ are plotted versus the azimuthally averaged isophotal radius, normalized by the radius at the 10 cts/pix isophote, R_{10} , for both a gas-poor (NGC 7518) and a gas-rich (UGC11524) galaxy. As can be seen in Fig. 3, the $\gamma(r)$ profiles are complex, and not readily described by a simple radial gradient in the SSFR. What is most striking about the two profiles is that the HI depleted galaxy actually has a high SSFR in its central region, while it is low everywhere else. On the other hand, $\gamma(r)$ is actually low in the central region of the HI-rich galaxy, but is high everywhere else. The contrast between $H\alpha$ and R band light in NGC 7518 versus in UGC11524 is further seen in the $H\alpha$ and R band images shown in Fig. 4.

To quantify the contrast in central SSFR between the high and low DEF galaxies, we have defined the quantity Δ , as follows:

$$\Delta = \gamma(0.1) - \Gamma, \quad (4)$$

where $\gamma(0.1)$ is the mean of the 10 highest values of $\gamma(r)$ found in the central $0.1R_{10}$ radius of the galaxy. Thus Δ represents the difference between this highest central value of $\gamma(r)$ and the global value Γ . A positive value of Δ indicates that the SSFR is higher in the center than it is globally; the global value is the average out to the 10 cts/pix radius R_{10} .

We have determined Δ for the 37 galaxies in which 10 valid data points are available within $0.1R_{10}$; the Δ values are given in column (10) of Table 2, while the $\gamma(0.1)$ values are in column (9). In Fig. 6 the Δ values are plotted versus DEF. In addition to a considerable scatter in the plot, a significant correlation between Δ and DEF is found. Specifically, a linear least squares fit yields a slope of 0.79 ± 0.17 and the correlation coefficient is 0.66. The hypothesis that the two variables are uncorrelated is rejected at the 3.5×10^{-5} level.

A perhaps surprising result is that the scatter around the fit between Δ and DEF is actually lower at high DEF than it is at low DEF. This is in contrast to our previous examination of the fit between global Γ^* and DEF, where the scatter around the fit at high DEF is greater than at low DEF. In Fig. 6 there appears to be a transition at $DEF \sim 0.3$ such that at $DEF \gtrsim 0.3$ all galaxies have a high value of Δ , i.e., centrally concentrated star formation, and the scatter around a linear trend between Δ and DEF is small. For $DEF < 0.3$, no significant trend is found between Δ and DEF, and the scatter in Δ is nearly a factor of 2 greater.

An additional look at the central SSFRs in our sample is provided in Fig. 7, where $\gamma(0.1)$ is plotted against DEF, i.e., we simply plot the $\gamma(0.1)$ measure of the highest central SSFR, without differencing it with the global value. While in Fig. 6 *all* galaxies with $DEF \gtrsim 0.3$ have high Δ values, in Fig. 7 the high DEF galaxies appear to bifurcate into a high $\gamma(0.1)$ and a low $\gamma(0.1)$ group. The high $\gamma(0.1)$ group of 6 galaxies, that lie within the dashed region in the upper right of Fig. 7, have higher $\gamma(0.1)$ values than nearly all of the low DEF galaxies, while the opposite is true for the low $\gamma(0.1)$ group. Remarkably, then, the HI-deficient high $\gamma(0.1)$ galaxies actually have higher central SSFR than typical gas-rich galaxies. While the remaining low $\gamma(0.1)$ galaxies at high DEF have lower central SSFR than gas-rich spirals, their SSFR is so low globally that they still have high Δ values.

The radial $\gamma(r)$ SSFR profiles for the 6 high $\gamma(0.1)$ gas-poor galaxies are shown in Fig. 8. With the exceptions of NGC 7074 and UGC12535, the central region of elevated SSFR is highly centrally concentrated. However, without emission line diagnostics, one cannot assume that the $H\alpha$ (and $[NII]\lambda 6548, 6584$) emission is due to star formation, as opposed to an active galactic nucleus (AGN). As is discussed in §2.4 we acquired optical

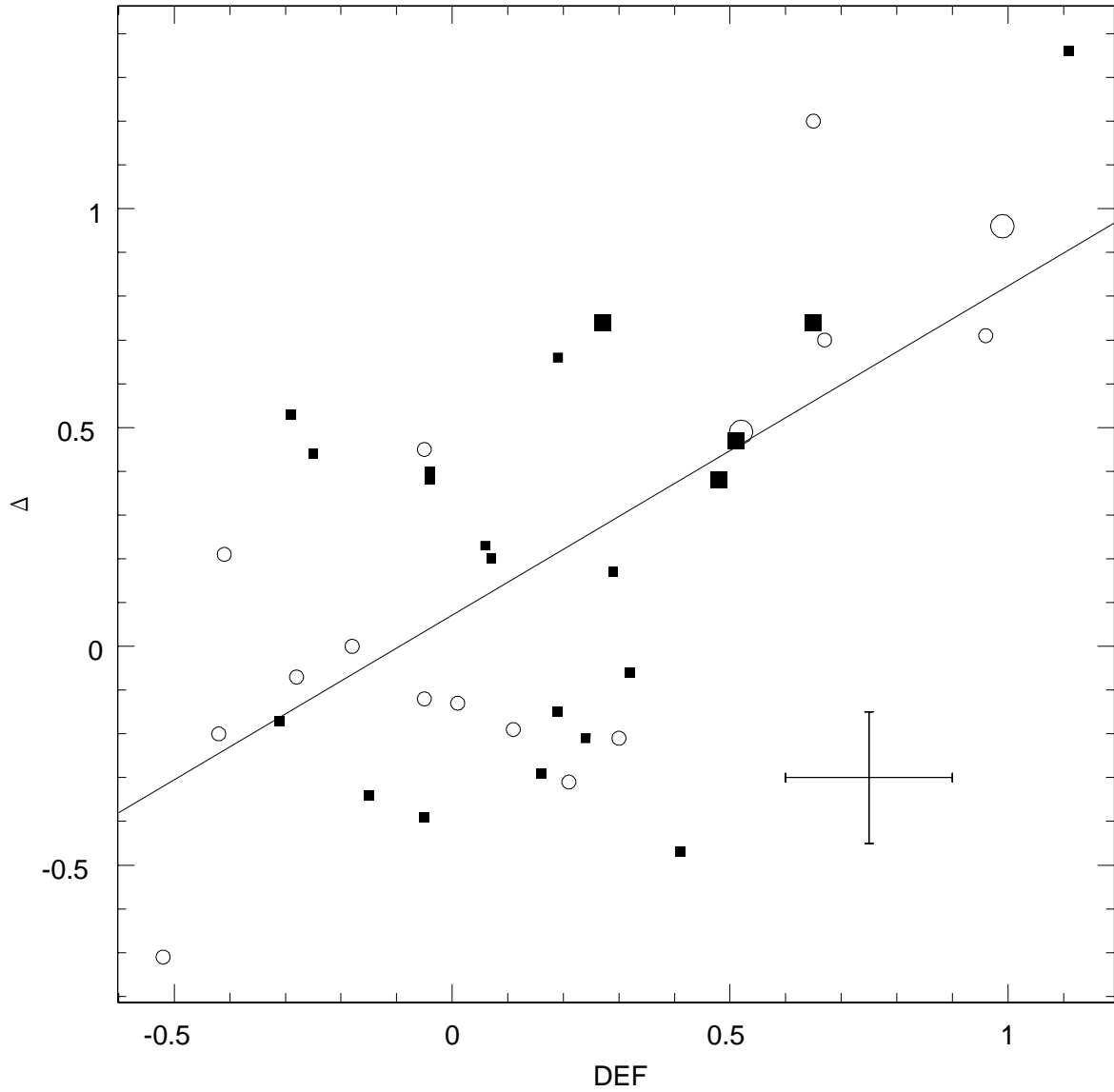


Fig. 6.— The Δ parameter, representing the difference in logarithmic SSFR between the central and global values (defined in §3.2), is plotted versus DEF for the galaxies in our sample with measurable values for Δ . The least squares fit to the data is denoted by the solid line. All symbols are the same as in Fig. 5.

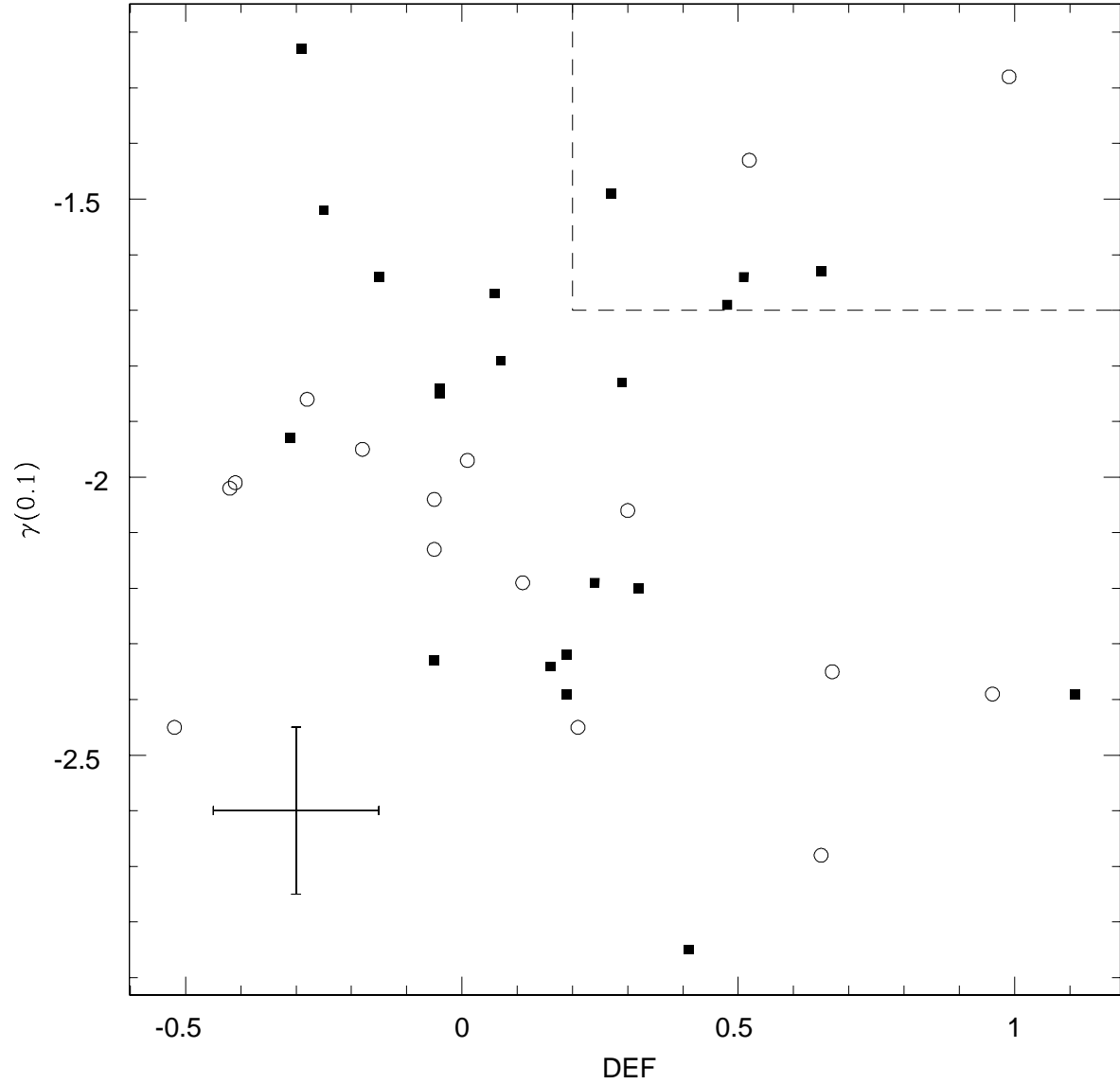


Fig. 7.— The maximum central SSFR parameter, $\gamma(0.1)$ (defined in §3.2), is plotted versus DEF for the galaxies in our sample. Filled squares and open circles are for Pegasus I cluster and non-cluster galaxies, respectively. The dashed box region in the upper right corner isolates the HI deficient galaxies with high peak central SSFR.

spectra of three of the high $\gamma(0.1)$ galaxies, NGC 7518, NGC 7643, and UGC164, covering both $H\alpha$ and $H\beta$, including the $[\text{NII}]\lambda 6548,8584$ and $[\text{OIII}]\lambda 4959,5007$ lines near $H\alpha$ and $H\beta$ respectively. The line ratios $[\text{OIII}]\lambda 5007/H\beta$ and $[\text{NII}]\lambda 6584/H\alpha$ are useful diagnostics for distinguishing between AGN/LINER spectra and HII region spectra due to star formation (e.g., Baldwin, Phillips, & Terlevich 1981). In Fig. 9 the nuclear spectrum of UGC164 is plotted. While $H\alpha$ is more than a factor of 2 greater than $[\text{NII}]\lambda 6584$, the excitation is very low, i.e., $[\text{OIII}]\lambda 5007$ is barely detected, while $H\beta$ in emission clearly rises well above the underlying $H\beta$ absorption in the integrated stellar spectrum. The combination of low excitation ($[\text{OIII}]\lambda 5007/H\beta=0.17$) and $H\alpha$ approximately twice $[\text{NII}]\lambda 6584$ unambiguously distinguishes the nuclear emission spectrum of UGC164 as that of a metal-rich HII region in Fig. 5 of Baldwin, Phillips, and Terlevich (1981). A similar conclusion is arrived at for NGC 7518 and NGC 7643. Thus for the three high DEF spirals with centrally concentrated $H\alpha$ emission for which we have optical spectra, we conclude that the emission is indeed due to high levels of star formation, rather than from an AGN.

To obtain further perspective on the high DEF galaxies with high $\gamma(0.1)$, we compare their radial $\gamma(r)$ profiles with those of gas-rich galaxies having a variety of $\gamma(0.1)$ values. In Fig. 10 are plotted $\gamma(r)$ profiles for gas-rich galaxies with both high central SSFR of $\gamma(0.1)>1.7$ (upper panel) and “typical” central SSFR of $\gamma(0.1)\sim 2$ (lower panel). The profile for NGC 7580 (Fig. 10a) shows the more spatially extended high SSFR that is also seen in two of the six gas-poor high $\gamma(0.1)$ galaxies, NGC 7074 and UGC12535. NGC 7580 is a Markarian galaxy, i.e., UV-excess on low-dispersion objective prism plates (Markarian 1967), and is included in a list of starburst nucleus galaxies in Coziol (2003). While neither NGC 7074 and UGC12535 are Markarian galaxies, NGC 7074 is described as a “post-eruptive” triplet in Zwicky (1971). In contrast, NGC 7591 (Fig. 10(b)) has a centrally concentrated SSFR peak, is also a Markarian galaxy, but its optical emission-line spectrum is characterized by Veron, Goncalves, and Veron-Cetty (1997) as composite LINER and HII region. NGC 7610 (Fig. 10(c)) is seen to have a high SSFR core, but more striking is the high $\gamma(r)$ throughout the disk. Its nuclear emission spectrum has been characterized as AGN by Schombert (1998).

Finally, we note that if the high DEF galaxies with high $\gamma(0.1)$, i.e., the galaxies with high absolute central SSFRs, are removed from consideration, the correlation between Δ and DEF is still present, with a slope of 0.68, a correlation coefficient of 0.55, and a probability that the two parameters are uncorrelated rejected at the 0.0015 level. Thus the correlation between Δ and DEF plotted in Fig. 6 is not just an effect produced by the high DEF galaxies with high $\gamma(0, 1)$.

In summary, gas-poor galaxies have higher SSFR in their centers relative to the average disk value (i.e., higher Δ), than do gas-rich galaxies. In fact, approximately half of the gas-

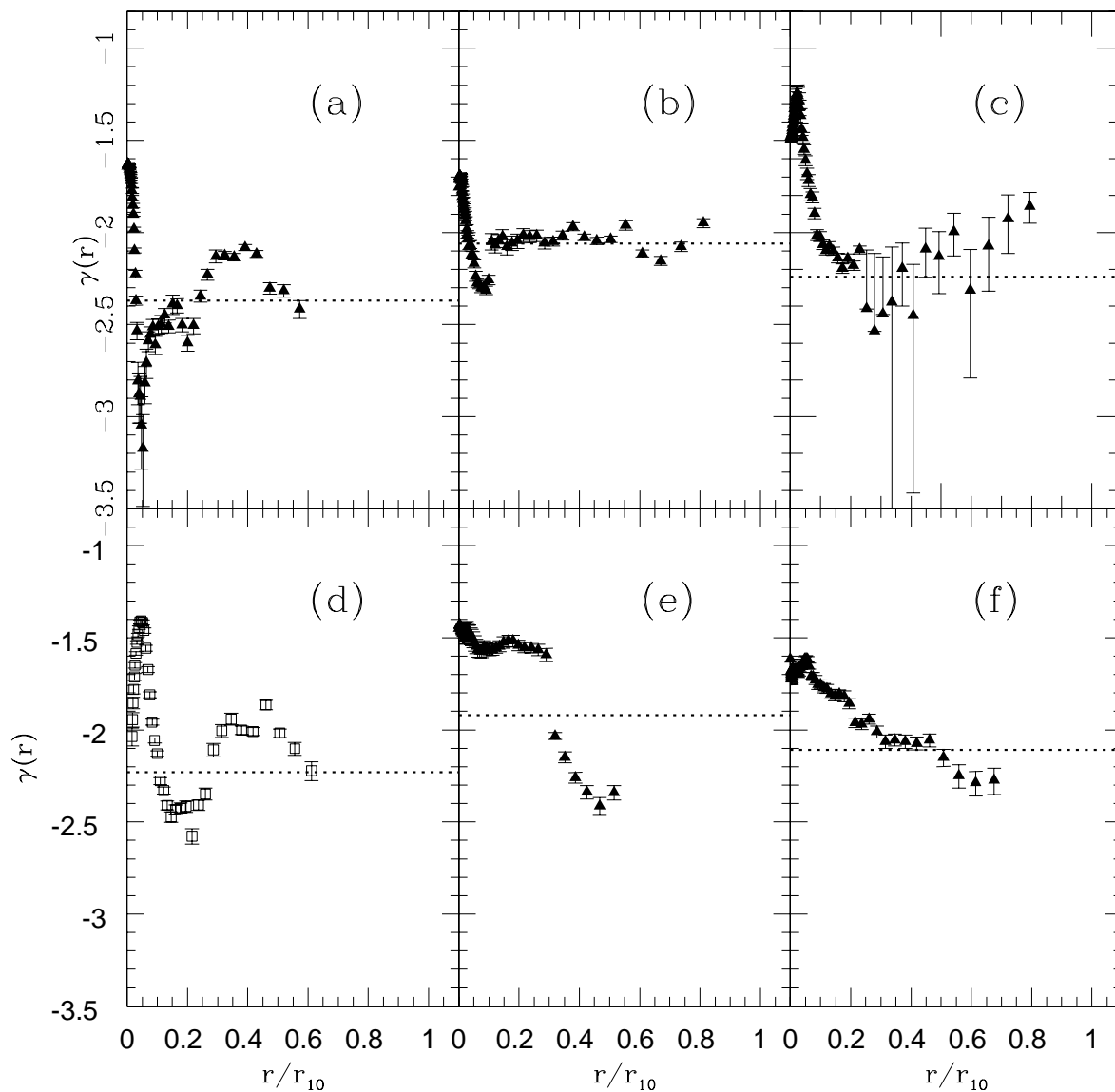


Fig. 8.— Radial $\gamma(r)$ SSFR profiles are plotted for the six high DEF galaxies with high central SSFR, $\gamma(0.1)$. The six galaxies are: (a) NGC 7518, (b) NGC 7608, (c) UGC164, (d) NGC 7643, (e) NGC 7074, and (f) UGC12535. The error bars correspond to the 1σ errors in both the R and H α fluxes, combined in quadrature. The horizontal dashed line in each panel represents the global value of the H α to R band flux ratio for that galaxy.

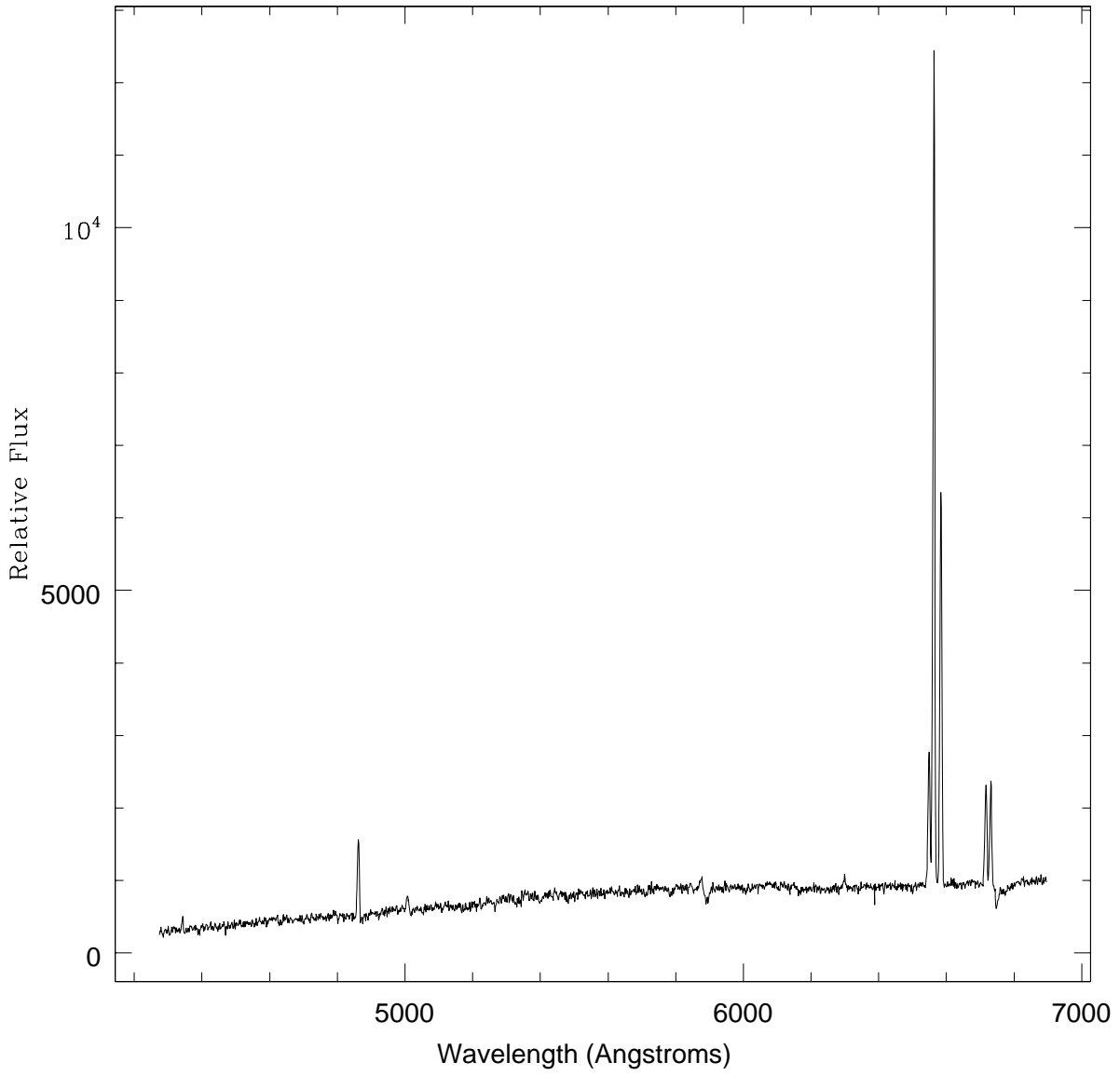


Fig. 9.— Deredshifted optical spectrum of UGC164.

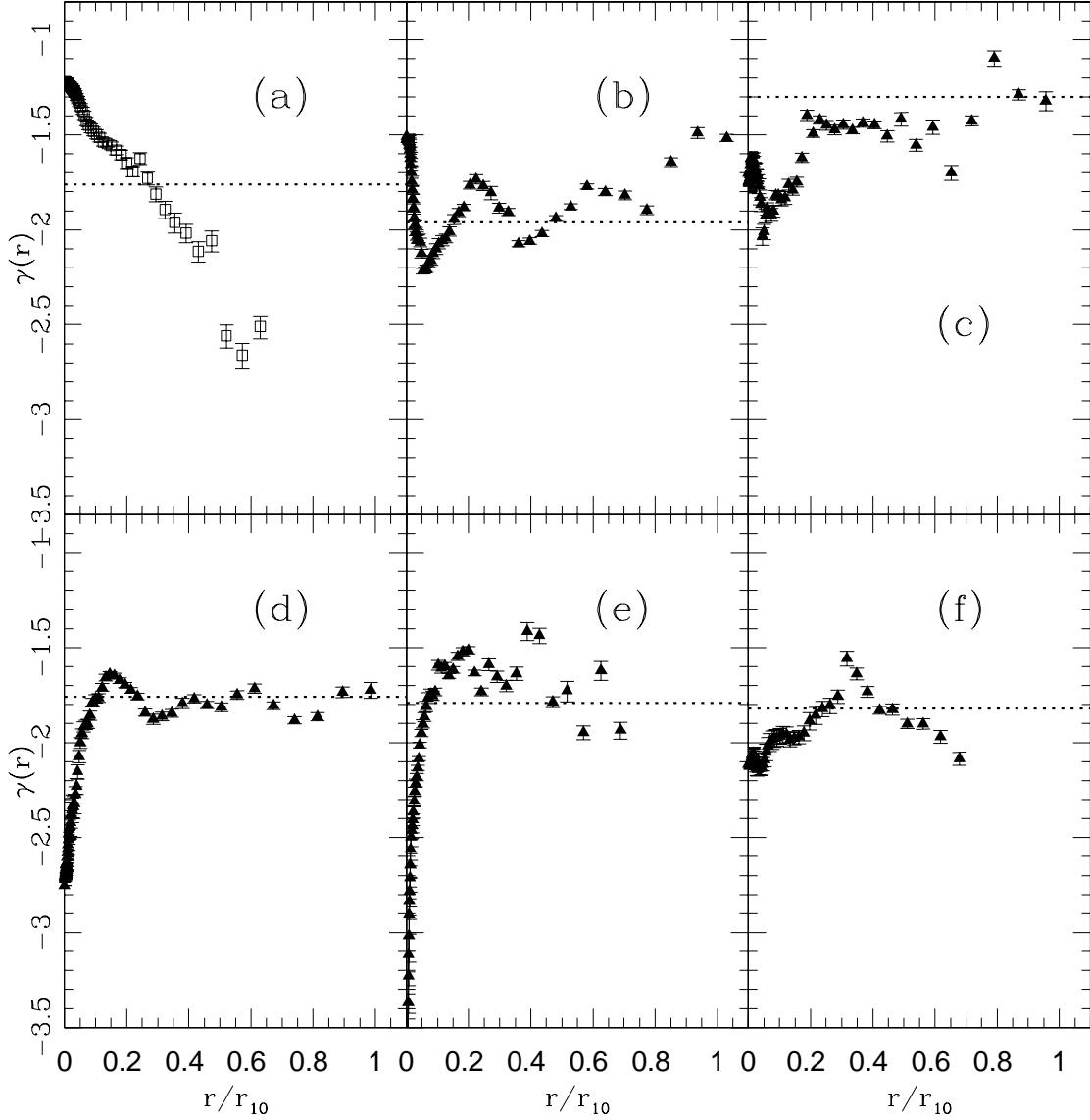


Fig. 10.— Radial $\gamma(r)$ SSFR profiles are plotted for three low DEF (gas-rich) spirals with high central SFR in the upper three panels: (a) NGC 7580, (b) NGC 7591, and (c) NGC 7610. Low DEF spirals with more typical central SFR of $\gamma(0.1) \sim -2$ are plotted in the lower panel: (d) IC 1205, (e) UGC11759, and (f) NGC 7537. The error bars correspond to the 1σ errors in both the R and H α fluxes, combined in quadrature. The horizontal dashed line in each panel represents the global value of the H α to R band flux ratio for that galaxy.

poor galaxies have higher central SSFR (i.e., higher $\gamma(0.1)$) than is typical of the gas-rich galaxies. Optical spectroscopy of several of the gas-poor spirals with high central SSFR indeed establishes that the H α emission is due to SF, rather than to an AGN.

3.3. H α Disk Truncation

The preceding Section §3.2 on radial SSFR profiles has emphasized the elevated *central* H α levels found in many high DEF galaxies (in an otherwise low SSFR and gas-depleted disk). KK04b find a correlation between the size of the H α disk and that of the HI disk, with high DEF galaxies exhibiting truncated disks. Defining the radial extent of something as knotty as an H α flux distribution is challenging. In KK04b the H α disk length is defined as the radius containing 95% of the H α flux. Here we define the H α disk length to be the outermost radius at which the H α surface brightness is above the 0.5 cts/pix level (that is mentioned in §2.3.2 to be the flux level above which we can reliably trace the emission). We divide this H α disk radius by the R band radius, r_{10} , to create a normalized H α disk size, $r_{H\alpha}/r_{10}$. The H α -to-optical disk sizes are plotted versus DEF in Fig. 11, along with the linear least squares fit. The fit has slope of -0.28 ± 0.08 , a correlation coefficient $r = -0.48$, and rejects the hypothesis of no correlation at the 0.0016 level. Hence, we find a significant correlation between the H α -to-optical disk size, $r_{H\alpha}/r_{10}$, and HI deficiency, DEF, indicating a progressive radial truncation of the star-forming disk with increasing HI deficiency.

An additional question relating to the truncated H α disks is whether or not the SSFR in the active part of the disk is at normal levels. That is, are the disks producing stars at normal rates out to the radius at which they are truncated? To address this question we calculated the average $\gamma(r)$ within the radial region $0.2r_{10} < r < r_{H\alpha}$. Note that we exclude the inner $0.2r_{10}$ to avoid being affected by the high central SSFR in many of the gas-poor galaxies, thereby ensuring an unbiased average of the disk (as opposed to nuclear) SSFR. This average disk SSFR, $\Gamma_{H\alpha}$ (which is listed in column (11) of Table 2), is plotted in Fig. 12 and is well correlated with DEF; the slope of the relation is -0.49 ± 0.13 (the hypothesis of no correlation is rejected at the 0.006 level). In Fig. 13 $\Gamma_{H\alpha}$ is plotted against $r_{H\alpha}/r_{10}$, which reveals that these two parameters are highly correlated; the hypothesis of no correlation is rejected at the 2.6×10^{-6} level. Hence we can affirm that the local SSFR is suppressed in truncated disks.

A comparison of the slopes of the correlations between Γ^* and DEF (slope of -1.05 ± 0.17), between $r_{H\alpha}/r_{10}$ and DEF (slope of -0.28 ± 0.08), and between $\Gamma_{H\alpha}$ and DEF (slope of -0.49 ± 0.13), further reveals that local suppression in and truncation of the star forming disk both contribute equally to the global correlation between SSFR and DEF. Since

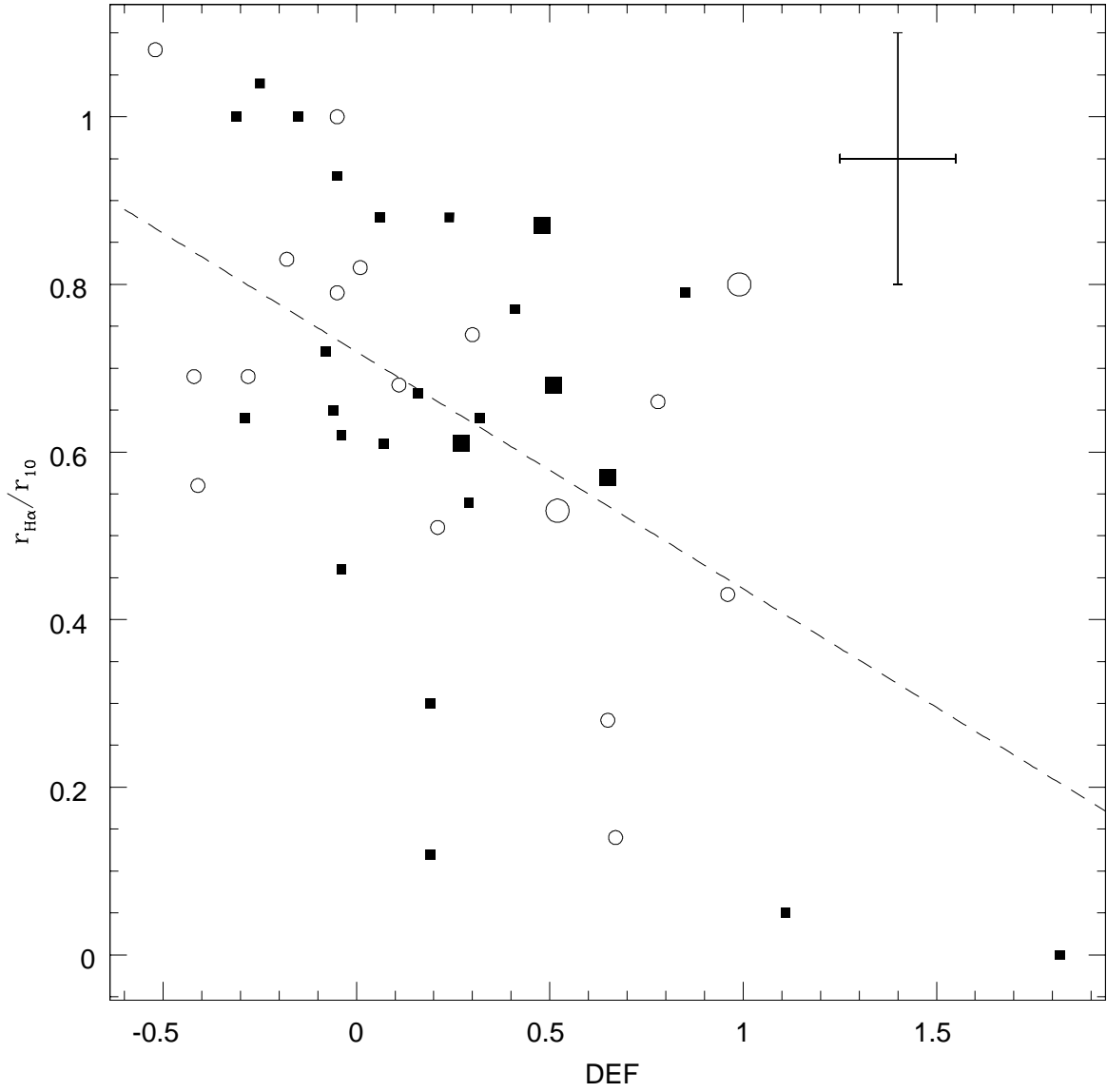


Fig. 11.— The H α -to-R band disk size ratio is plotted versus DEF. The dashed line represents the linear least squares fit to the data. All symbols are the same as in Fig. 5.

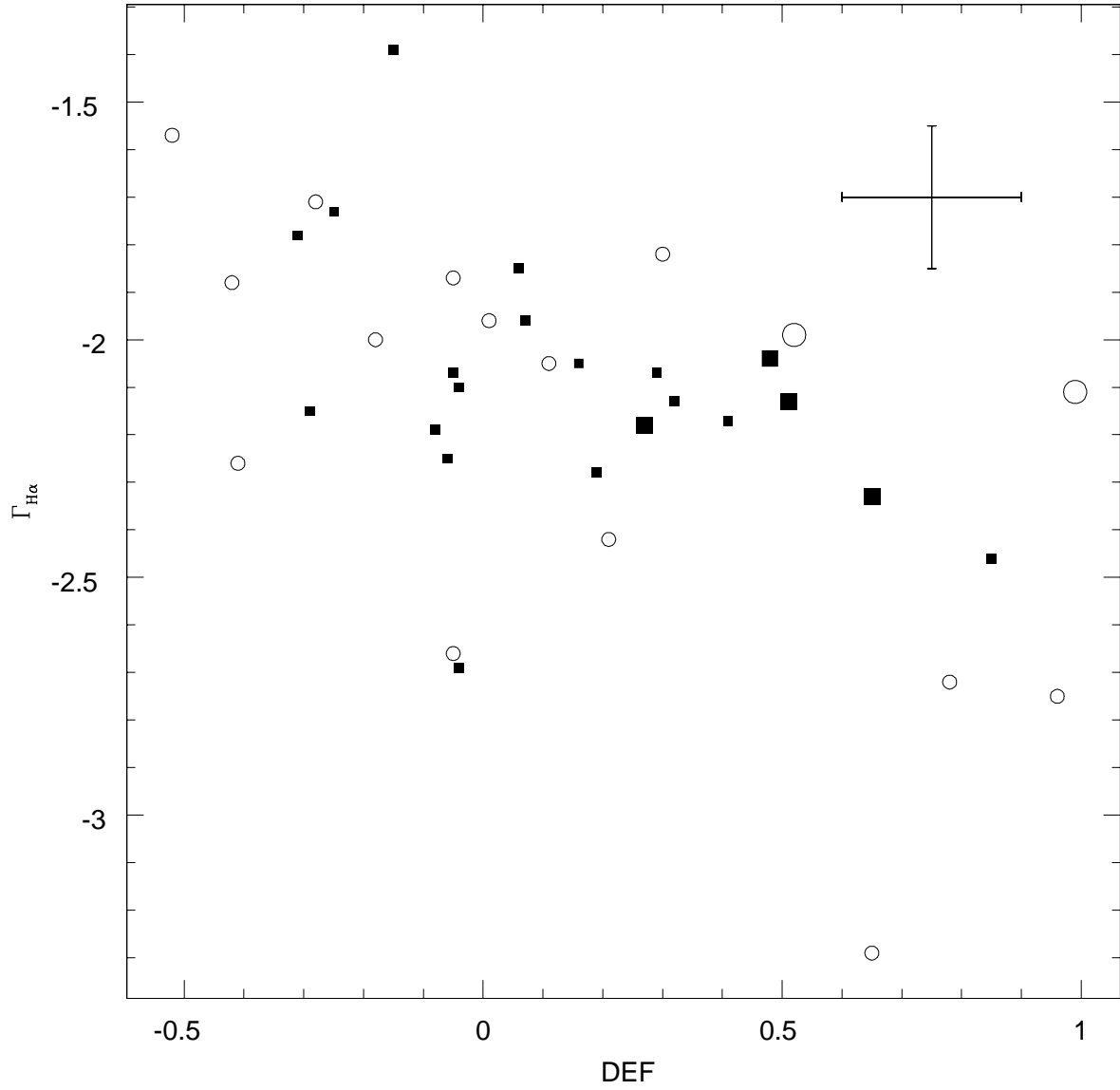


Fig. 12.— The average SSFR within the star-forming part of the disk, $\Gamma_{H\alpha}$ (defined in §3.3), is plotted versus DEF. All symbols are the same as in Fig. 5

$\text{SSFR} \sim (r_{H\alpha}/r_{10})^2$, then the fact that the square of the slope of the $r_{H\alpha}/r_{10}$ vs DEF correlation, $2(-0.28) = -0.56$, is within the errors equal to the -0.49 slope of the correlation between $\Gamma_{H\alpha}$ and DEF, indicates that the two trends contribute equally to the correlation between global SSFR and DEF. In addition, we can assume that SSFR is proportional to $\Gamma_{H\alpha}(r_{H\alpha}/r_{10})^2$. Thus the fact that the observed slope of Γ^* vs DEF, -1.06, is within the errors equal to $-0.49+2(-0.28)$ indicates that we have a single population of galaxies in which the star forming disks are *both* truncated and suppressed, rather than two populations, one truncated and the other suppressed.

3.4. Morphology of the High Central SFR Galaxies

While the preceding examination of the azimuthally averaged radial SSFR profiles provides quantitative data concerning the nature of HI deficient spirals, further insight on these galaxies is in principle contained in their detailed morphologies. We first return to Fig. 4, in which the R band and $H\alpha$ images of NGC 7518, a prototype for the HI-deficient galaxies with high central SSFR, are contrasted with those of UGC11524, a prototype for the gas-rich spirals. The $H\alpha$ image of NGC 7518 is clearly characterized by a bright emission core, and a ring of HII regions which are coincident with the end of the bar seen in the middle panel R band image. Furthermore, the $H\alpha$ emission is truncated at the end of the bar, while the faint outer R band light is seen to extend well beyond the $H\alpha$ disk. In contrast, for UGC11524 there is no bright $H\alpha$ emission core. In addition, the $H\alpha$ emission traces the R band light even to the faint outer spiral arms.

Two of the three other high DEF galaxies with a central $H\alpha$ emission core exhibit similar morphologies to NGC 7518, as is seen in Fig. 14. NGC 7643 in particular has a similar morphology, i.e., an emission core, a ring of HII regions that coincide with the end of a bar structure, and then a faint R band disk that extends well beyond the $H\alpha$ disk. UGC164 is similar as well, with a very bright $H\alpha$ emission core, and a clear stellar bar structure, with no $H\alpha$ emission evident beyond the bar. The faint R band light beyond the bar is difficult to characterize, however. The fourth galaxy, NGC 7608, is too close to edge-on to tell whether a bar structure is present, and whether the extranuclear HII regions form a ring.

Two other high DEF galaxies have elevated central SSFR. However, in these cases the bright emission extends outside the nucleus. In Fig. 15 R band and $H\alpha$ images are shown for these two galaxies, NGC 7074 and UGC12535. The HII emission in NGC 7074 forms the nearly linear triple structure noticed by Zwicky (1972). It appears that this galaxy is seen close to edge-on, thus no conclusion can be reached about a bar structure. However, it is also clear that the faint outer R band light extends well beyond the $H\alpha$ structure

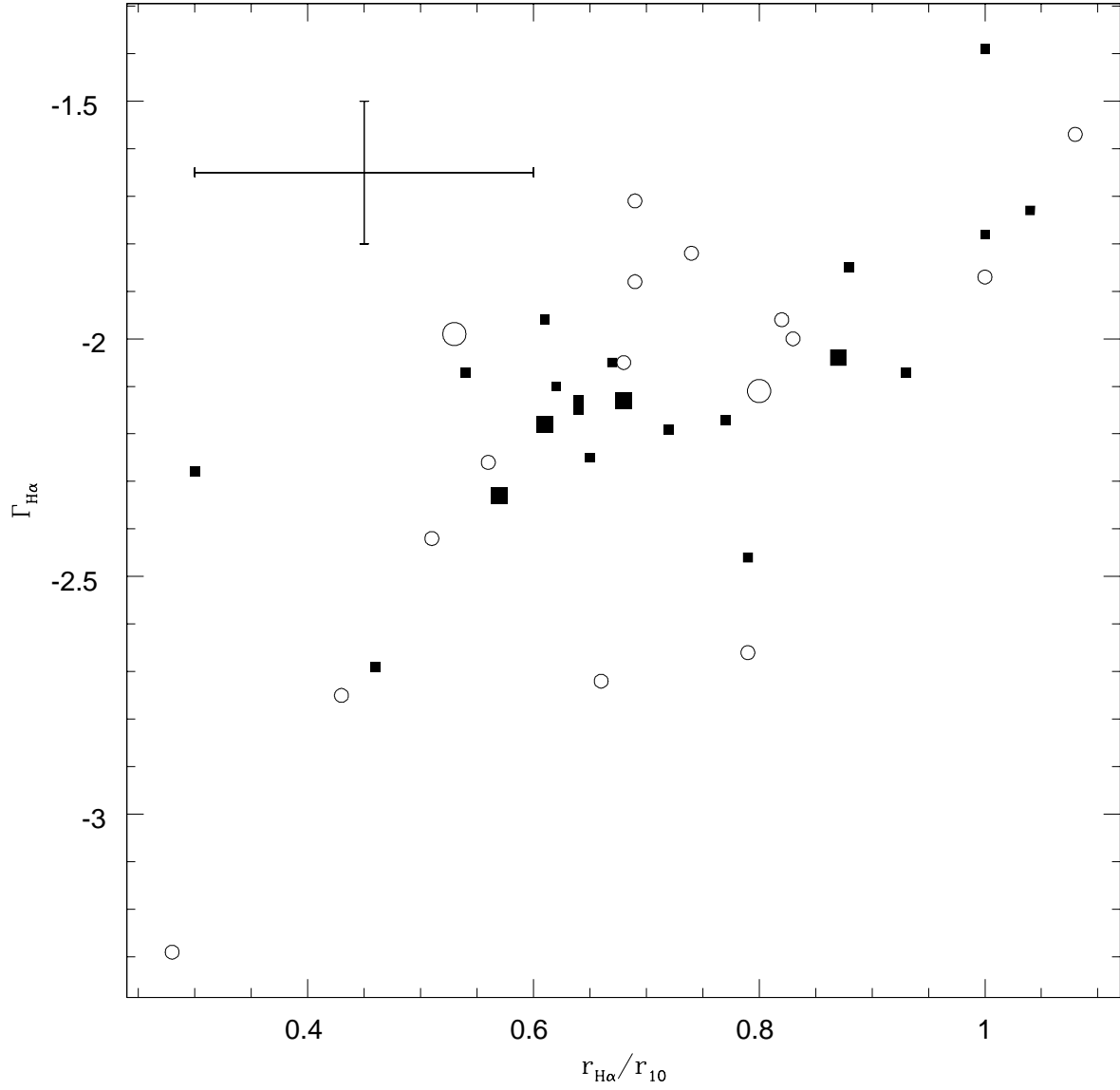


Fig. 13.— The average SSFR within the star-forming part of the disk, $\Gamma_{H\alpha}$, is plotted versus, $r_{H\alpha}/r_{10}$, the H α -to-R band disk size ratio. All symbols are the same as in Fig. 5.

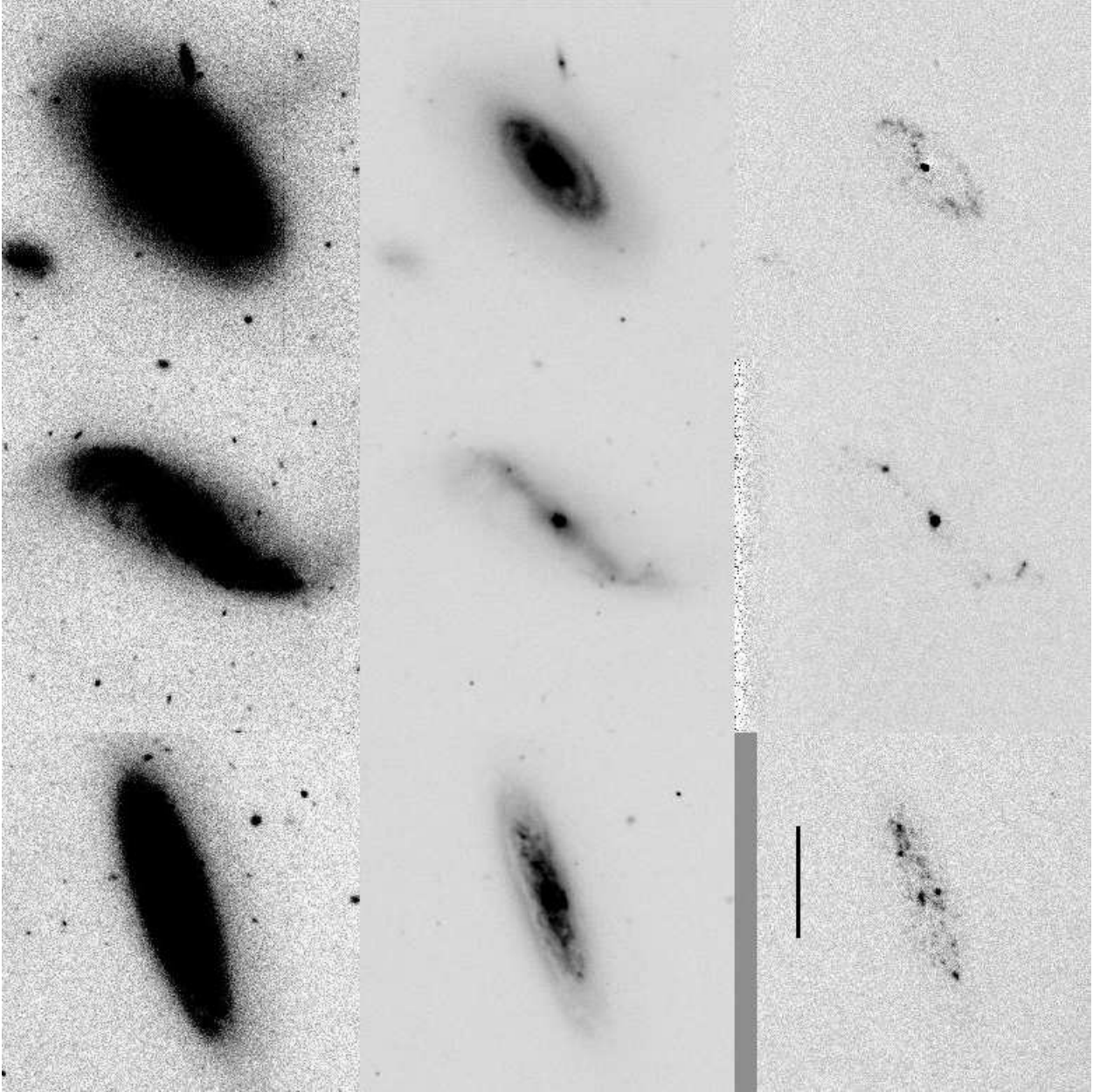


Fig. 14.— R band and $H\alpha$ images are displayed for three gas-poor spirals with bright central $H\alpha$ emission cores. NGC 7643 is in the upper panels, UGC164 in the middle panels, and NGC 7608 is in the lower panels. The R band images are shown at two contrast levels in the left and middle panels, while the $H\alpha$ image are shown in the right panels. The black line in the lower right panel indicates an angular scale of $30''$.

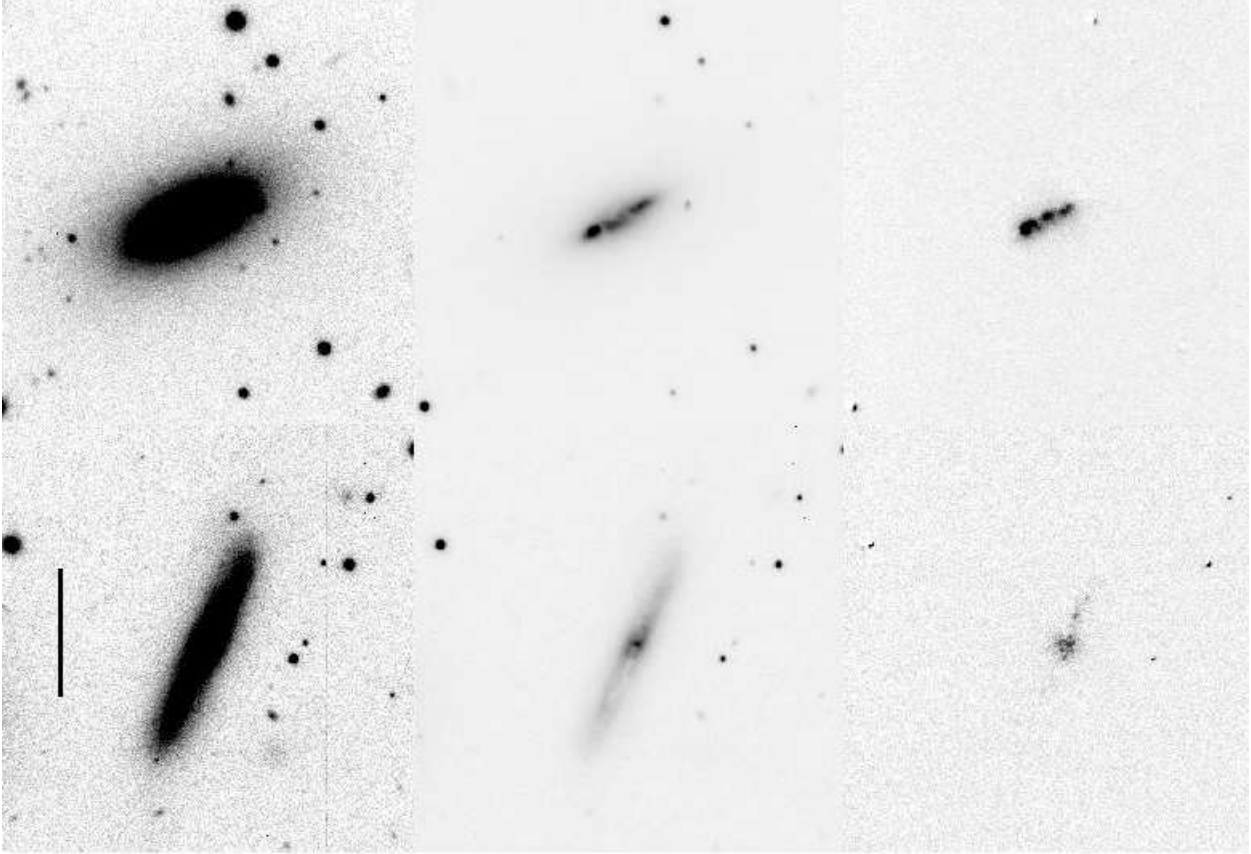


Fig. 15.— R band and $H\alpha$ images are displayed for two gas-poor spirals with extended bright central $H\alpha$ emission regions. NGC 7074 is in the upper panel and UGC12535 is in the lower panel. The R band images are shown at two contrast levels in the left and middle panels, while the $H\alpha$ images are shown in the right panels. The black line in the lower left panel indicates an angular scale of $30''$.

and is surprisingly regular. UGC12535 is seen almost perfectly edge-on, thus the inner HII morphology is not discernable.

3.5. Individual Galaxies

We conclude the discussion of SFR profiles in HI-deficient spirals by briefly investigating two individual cases of spirals whose complex H α morphologies are not adequately represented by an azimuthally averaged radial profile. R band and H α images for CGCG 059-019=AGC170317 and for UGC12497 are shown in Fig. 16. The H α emission in CGCG 059-019 is confined to an arc of HII regions along the SSE edge of this gas-poor ($DEF=0.65$) galaxy. The R band image reveals an inner bar and ring, surrounded by a single outer spiral arm. The H α emission traces just the southern edge of this arm. The asymmetry in the R band and H α emission is reminiscent of NGC 2276 in the NGC 2300 group (Davis et al. 1997). In that case, the similar asymmetry seen in both the stellar optical light and the H α light led Davis et al. (1997) to propose a tidal origin for the asymmetry in NGC 2276. In the case of CGCG 059-019, however, the appearance of a *single* outer spiral arm, as well as the almost perfect arc of HII regions, seems more consistent with a ram pressure event, such as the single leading spiral arm seen in the ram pressure numerical simulation of Tosa (1994, see also Schulz & Struck 2001). On the other hand, the Tosa (1994) simulation only follows the evolution of the gaseous disk. It appears unlikely that the stellar disk would exhibit the same asymmetric response. Nevertheless, in CGCG 059-019 the R band light clearly shows the m=1 single-arm pattern. Note that if the single arm is caused by the ram pressure effect modeled by Tosa (1994), then the galaxy disk must be oriented nearly parallel with respect to its motion relative to the intragroup gas. Hence the galaxy, according to the near circular appearance of the inner ring, must be moving almost exactly in the plane of the sky. CGCG 059-019 is a member of compact group #65 in the catalog of Focardi & Kelm (2002), which contains 7 galaxies and has a velocity dispersion of 329 km s⁻¹. Thus it appears to be in a similar group environment to NGC 2276 in the NGC 2300 group. In any case, if it can be established that the single arm in CGCG 059-019 is indeed leading, then it may represent a key object for distinguishing ram pressure from tidal effects in the group environment. Just as intensive studies of specific galaxies in rich clusters have led to unambiguous determinations of ram pressure effects (e.g., Kenney & Koopman 1999; Kenney et al. 2004; Vollmer et al. 2006), of tidal effects (Kenney et al. 1996), and of both (Yoshida et al. 2008), a further investigation of CGCG 059-019 may provide unambiguous clues to the mechanism producing the m=1 spiral pattern in that galaxy.

The other galaxy with exceptional morphology is UGC12497, also seen in Fig. 16. This

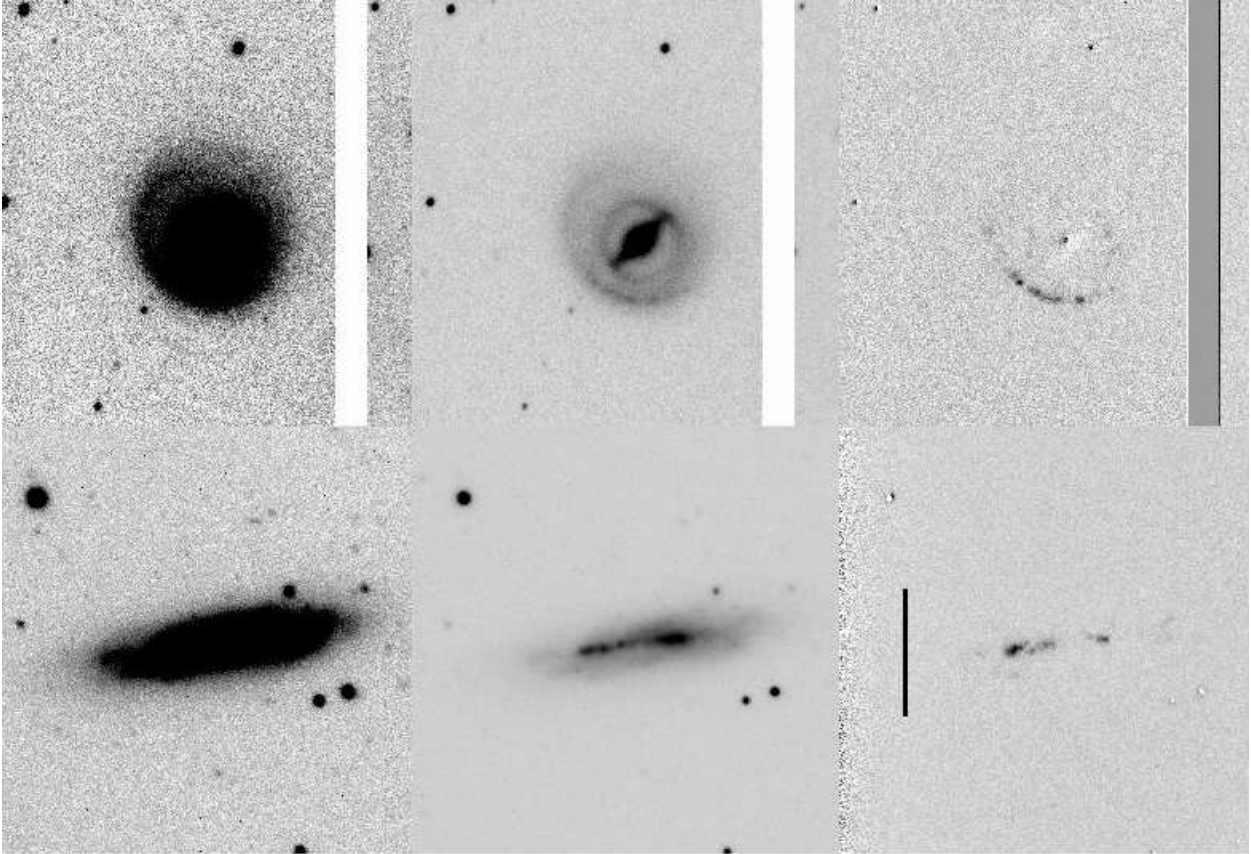


Fig. 16.— R band and $H\alpha$ images are displayed for two galaxies with unusual morphologies. CGCG 059-019 is in the upper panel and UGC12497 is in the lower panel. The R band images are shown at two contrast levels in the left and middle panels, while the $H\alpha$ images are shown in the right panels. The black line in the lower right panel indicates an angular scale of $30''$.

galaxy is a member of the central group of the Pegasus I cluster, and has been classified as Im. While the outer isophotes of the R band image do indeed look like those of a single object, both the inner R band isophotes and H α image are perhaps more indicative of two discrete spirals in the process of merging. If so, their line-of-sight relative velocity must be low at this point, since the HI profile width given by L07 is only 188 km s⁻¹. The HI profile, shown in Fig. 3.18 of L07, does have a small spike at ~ 3740 km s⁻¹, indicative of a second still-discrete galaxy.

4. Discussion

As was mentioned in the Introduction, both KK04ab and FG08 conclusively establish a relation between global SSFR and HI deficiency in Virgo cluster spirals, but disagree as to whether truncation of the star-forming disk or global quenching in SSFR is the more important driver. FG08 argue that disk quenching is the key process in Virgo cluster spirals while KK04ab find that truncation is important in approximately half of their Virgo spirals. We now consider how the results of our study impact on the issue of disk truncation versus disk quenching.

In this study we have found that the relation between global SSFR and atomic gas deficiency is evident as well in the Pegasus I cluster and in other low-richness environments. Naturally, it is an oversimplification to compare the “Pegasus environment” with that of the “Virgo environment”, since an individual Virgo cluster galaxy may have experienced a wide range of different environmental histories over the past ~ 10 Gyr, depending on the specifics of its group membership and orbital path through the greater cluster. Nevertheless, galaxies in the Pegasus I cluster and in the “non-cluster” sample on average have experienced an environment that has a considerably lower peak ram pressure (due to both lower galaxy velocity dispersion and to lower density of the ICM) than for Virgo. Thus it is interesting to see the correlation between global SSFR and DEF that is found in Virgo continue in the environments inhabited by our galaxy sample.

Regarding the issue of truncation versus starvation of disks, our results indicate a steady reduction in star-forming disk length with increasing DEF. This result, which is consistent with that found by KK04b in Virgo cluster spirals, implies that gas is being preferentially removed from the outside of stellar disks by the processes at work in the less extreme environments sampled in our study. In comparing our results to that found by FG08 for Virgo spirals, it is perhaps important that FG08 considered highly luminous galaxies, while the typical galaxy in our sample is ~ 1 - 1.5 mag less luminous. In addition, the spirals with truncated disks also have lower SSFR within the actively star-forming part of the disk than do

gas-rich spirals with normal size disks.

An important difference between our results and that found previously in the Virgo cluster environment is the high ($\sim 50\%$) fraction of spirals with $\text{DEF} \gtrsim 0.2$ that have high central SSFR. KK04b find three Virgo spirals with high DEF that have severely truncated $\text{H}\alpha$ disks, but high central SFR. All three galaxies have M_B between -18 and -19, which is typical of our sample, but substantially fainter than the luminous spirals studied by FG08. The three KK04b examples have higher DEF (0.79, 1.23, and >1) and more severely truncated $\text{H}\alpha$ disks than in our sample, but otherwise appear to have similar characteristics. However, those three galaxies only constitute $\sim 8\%$ of the Virgo spirals studied by KK04b, while we find that $\sim 50\%$ (although the number statistics are small) of our spirals with $\text{DEF} \gtrsim 0.2$ have high central SSFR. The two noteworthy differences between our galaxy sample and the Virgo sample of KK04b are that (1) our galaxies are typically less gas-depleted than the Virgo spirals, by about a factor of 2-4, and (2) the environments inhabited by our sample are poor clusters and groups, as opposed to the denser Virgo environment.

The elevated SSFR in the centers of many partially HI-depleted spirals poses a particularly interesting problem. Without an ongoing HI resupply, such high (an order of magnitude higher than in normal spirals) central SSFRs are unsustainable, and thus indicate a transient evolutionary state. There are a number of galaxies in Pegasus I which may in fact represent end products of this transient state of high central SSFR. Vigroux, Boulade, & Rose (1989) found several galaxies in Pegasus, classified as early-type, but with spectroscopic evidence of recent (NGC 7557, NGC 7611, and NGC 7617) or still ongoing (NGC 7648) central star formation. Optical broadband imaging presented in Rose et al. (2001) further indicates recent centralized star formation. NGC 7648 may be a particularly relevant example. In addition to the broadband data in Rose et al. (2001), B, R, and $\text{H}\alpha$ imaging in L07 reveals that despite its S0 classification, NGC 7648 has highly centrally concentrated $\text{H}\alpha$ emission, a bright off-nuclear blue knot, and ripples reminiscent of tidal interaction. The peaked HI profile for NGC 7648 suggests that the small amount of remaining HI is not in a cold rotating disk, thus probably also centrally concentrated. All of these characteristics indicate that NGC 7648 may represent the last transition stage before evolution into an S0. The data for NGC 7563 presented in this paper are also indicative of a pre-S0 state. Neither HI nor $\text{H}\alpha$ are detected in this galaxy, but the central morphology is sufficiently structured that it has been classified as an Sa. In fact, both NGC 7643 and NGC 7563 are likely examples of the “problem” of galaxy morphology emphasized by Koopmann & Kenney (1998). HI-deficient galaxies in clusters tend to be mis-classified as earlier types than their central concentration parameters would indicate. Naturally, once a disk galaxy becomes completely depleted in atomic and molecular gas, it will eventually be classified as an S0, and then no longer be considered in samples of HI deficient galaxies, which are restricted to Sa and later types.

Both NGC 7648 and NGC 7563 appear to be on the brink of the S0/a morphology.

We note other possible examples of cluster galaxies with elevated central SFR. In an objective prism survey of eight nearby galaxy clusters, Moss & Whittle (1993, 2000, 2005) find numerous spirals with centrally concentrated H α emission. In addition, Caldwell et al. (1993) and Caldwell & Rose (1997) find examples of “early-type” galaxies in nearby clusters that have spectroscopic evidence for recent star formation. Long-slit spectroscopy (Caldwell et al. 1996; Rose et al. 2001) and *HST* imaging (Caldwell, Rose, & Dendy 2003) indicate that the recent star formation has been concentrated in the inner ~ 2 kpc of these galaxies. Bothun & Dressler (1986) studied blue compact star-forming disk galaxies in the Coma cluster. However, these spirals have elevated SFR throughout their truncated star-forming disks, which is distinct from our spirals that have truncated star-forming disks but *lower* SFR within the active disk, except for the very central region of elevated SFR.

In closing, we return to the key question regarding whether ram pressure and/or tidal gravitational effects are primarily responsible for the HI depletion in disk galaxies in poor cluster and group environments. Have the data presented here informed this question in any decisive way? We begin by summarizing the five principal conclusions from this study that are pertinent to the issue. First, the *global* SSFR is correlated with DEF, i.e., lowered SSFR accompanies higher atomic gas depletion. Second, there is a clear correlation between the H α -to-optical disk size ratio with DEF, i.e., more HI-deficient galaxies have more truncated disks. Third, truncation *and* suppression of SSFR (within the star-forming part of the disk) are both seen in the same disks, and contribute about equally to the SSFR-DEF correlation. Fourth, the central SSFR is greatly enhanced in some high DEF galaxies. Fifth, strong bars and a ring of HII regions at the end of the bar appear to be present in the high DEF galaxies with high central SSFR. Finally, these effects are observed by us in the poor cluster and group environment.

Are ram pressure stripping (RPS) and/or tidal effects consistent with these observational trends? Let us first consider the case of strong RPS. One might expect that with strong RPS the disk will be HI-depleted in proportion to the strength of the ram pressure. Thus a correlation between H α -to-optical disk size ratio might be expected, in addition to a correlation between global SSFR and DEF. Thus the first two effects, and probably the third, will result in the strong RPS case. On the other hand, it is not clear why the fourth and fifth effects would be observed. Bar structure and highly elevated central SFR are expected in the event that a non-axisymmetric structure is triggered; strong RPS does not obviously provide that trigger. And the fact that we observe the various effects in galaxies in such low density environments is inconsistent with strong RPS.

Tidal interaction will naturally trigger non-axisymmetric disturbances, which will read-

ily lead to the bar structures and high central SSFR. On the other hand, it is not all clear how the H α -to-optical disk size ratio correlation with DEF will result. A tidal disturbance will tend to provide non-axisymmetric disturbances whose scale is *internally* set (by the location of the inner Lindblad resonance, i.e., by the internal mass distribution and resultant rotation curve), rather than by the strength of the tidal disturbance. Thus the H α disk truncation radius will not obviously correlate with the magnitude of the disturbance, which presumably correlates with DEF. Thus both strong RPS and tidal disturbances appear to have opposite strengths and weaknesses when confronted by the observations. The case of weaker RPS represents a potentially interesting middle ground. Schulz & Struck (2001) find that weaker RPS leads to an atomic gas disk compression that in turn is unstable to growth of non-axisymmetric structure, which results in the “annealing” of the disk, i.e., a shrunken disk of atomic gas. Thus weak RPS does produce a truncation of the disk. What is not clear, however, is whether the degree of the truncation will correlate with the strength of the ram pressure or whether, like in the case of tidal perturbations, one expects the scale to be set internally, by the nature of the galaxy’s rotation curve. Also unclear is whether the SSFR in the star-forming part of the disk will be suppressed. The disk annealing should in any event be accompanied by bar structure, gas inflow, and an elevated SSFR.

In short, there is considerable “degeneracy” in behavior between RPS-induced and gravitationally-induced disk evolution. Both mechanisms are capable of redistributing the angular momentum of the gas such that gas is driven to the galaxy centers, and both are capable of selectively removing the outer gas supply. Consequently, although the observational results presented here provide some interesting new constraints on any model for gas removal in disk galaxies, we do not see a clear signature at this point for any single mechanism.

5. Conclusions

We have obtained H α and R band imaging of 29 spiral galaxies in the spiral-rich Pegasus I cluster and of 18 spirals in non-cluster environments. The H α image is used to track the SFR, while the R band roughly tracks the total stellar light, and hence the stellar mass. We compare the logarithmic H α to R band flux ratio (i.e., the logarithm of the SFR per unit stellar mass, or SSFR) to the logarithmic HI deficiency parameter, *DEF*, for our sample of disk galaxies. We find that global SSFR is well correlated with HI deficiency, from the most HI-rich to the most HI-poor galaxies, in the expected sense that gas-poor galaxies have lower global SSFRs. This establishes in lower density environments the same connection between HI deficiency and lowered SFR that has been observed before in rich clusters such as Coma and Virgo. We also find that the H α disk size relative to the R band disk size correlates

with *DEF*, i.e., H α disks are truncated relative to the optical disk size in more gas-poor spirals. If the SFR in the nuclear region of the galaxy is excluded, we find that the SSFR within the H α disk is reduced in HI deficient galaxies. Thus gas-depleted galaxies not only have a smaller H α disk with increasing HI deficiency, but the SSFR within the star-forming part of the disk is also lower. However, for approximately half of the gas-poor galaxies, the central SSFR is greatly elevated relative to that in gas-rich spirals. Furthermore, the SSFR in the nucleus relative to the global value in the galaxy *increases* with HI deficiency. These high nuclear SSFRs in partially HI-depleted galaxies point to a transient evolutionary state in which gas is efficiently transported to the central region. Whether the condition is triggered more readily by ram pressure effects, or whether the origin lies with gravitational perturbation, remains to be seen. We also note the special case of CGCG 059-019, a one-armed spiral with a nuclear ring and bar, in a small galaxy group. The m=1 pattern may be the direct result of a ram pressure wind parallel to the galaxy's disk. Finally, since global and local SFRs in spirals are so clearly coupled to HI depletion, and since the SFR (through H α imaging) and kinematics of star-forming regions can be studied at higher spatial resolution than the HI distribution, H α imaging and kinematics provide a particularly powerful probe of the mechanisms driving disk galaxy evolution.

We wish to thank the anonymous referee for suggestions that have substantially improved the final paper.

Table 1. Galaxy Properties

(1) Name	(2) Alt Name	(3) RA	(4) DEC	(5) Type	(6) cz	(7) Log Density
Non-Pegasus Galaxies						
NGC 41	AGC 100086	00:12:48.0	+22:01:24	5	5949	-1.75
UGC 144	—	00:15:26.8	+16:14:07	4	5620	-1.60
UGC 164	—	00:17:23.7	+18:05:03	4	5443	-0.63
NGC 352	AGC 400553	01:02:09.2	-04:14:44	3	5284	-1.46
UGC 1026	—	01:27:13.0	+13:36:08	9	4505	-1.98
IC 1721	UGC 1187	01:41:24.4	+08:31:32	3	4299	-2.53
CGCG 059-019	AGC 170317	08:01:54.1	+09:37:33	4	4793	-1.28
NGC 5417	UGC 8943	14:02:13.0	+08:02:14	1	4879	-2.03
IC 1132	UGC 9965	15:40:06.7	+20:40:50	5	4259	-1.86
NGC 5990	UGC 10024	15:46:16.3	+02:24:56	1	3839	-2.45
IC 1205	AGC 260337	16:14:15.9	+09:32:14	2	3240	-2.54
UGC 11524	—	20:12:03.9	+05:45:49	5	5257	-1.42
CGCG 373-007	AGC 300178	20:26:14.7	+01:06:11	5	3708	-2.18
NGC 7074	AGC 310103	21:29:38.8	+06:40:57	2	3476	-2.36
NGC 7081	UGC 11759	21:31:24.1	+02:29:29	3	3273	-2.49
CGCG 402-018	AGC 310171	21:45:58.8	+07:52:18	4	3754	-2.32
UGC 11848	—	21:55:35.2	+10:27:59	8	4992	-2.59
UGC 12479	—	23:17:25.7	-01:35:10	1	4206	-2.53
Pegasus I Cluster Galaxies						
UGC 12304	—	23:01:08.3	+05:39:16	5	3470	-0.94
UGC 12361	—	23:06:22.4	+11:17:08	10	2992	-1.60
UGC 12370	—	23:07:06.3	+09:57:39	6	4892	-1.77
IC 1474	UGC 12417	23:12:51.3	+05:48:23	6	3506	-0.20
NGC 7518	UGC 12422	23:13:12.7	+06:19:18	1	3071	-0.34
NGC 7529	UGC 12431	23:14:03.2	+08:59:33	4	4538	-1.54
NGC 7537	UGC 12442	23:14:34.5	+04:29:54	4	2674	-1.60
NGC 7541	UGC 12447	23:14:43.9	+04:32:04	5	2689	-1.49
UGC 12451	—	23:14:45.2	+05:24:47	10	3645	-0.94
NGC 7563	UGC 12465	23:15:55.9	+13:11:46	1	4174	-1.00
UGC 12467	NGC7562A	23:16:01.4	+06:39:08	8	3507	-0.39
CGCG 406-042	AGC 330179	23:17:05.5	+07:07:22	5	3564	-0.56
NGC 7580	UGC 12481	23:17:36.4	+14:00:04	4	4434	-0.97
NGC 7593	UGC 12483	23:17:57.0	+11:20:57	5	4108	-1.46
NGC 7591	UGC 12486	23:18:16.3	+06:35:09	4	4956	-1.49
UGC 12494	AGC 331419	23:18:52.6	+06:52:38	7	4196	-1.62
UGC 12497	—	23:19:10.8	+07:42:13	10	3761	-0.47
IC 5309	UGC 12498	23:19:11.6	+08:06:34	3	4198	-1.37
NGC 7608	UGC 12500	23:19:15.3	+08:21:01	4	3508	-0.17
NGC 7610	UGC 12511	23:19:41.4	+10:11:06	6	3554	-0.57
NGC 7615	AGC 330237	23:19:54.4	+08:23:58	3	4473	-1.33
UGC 12522	—	23:20:16.6	+08:00:20	9	2812	-1.29

Table 1—Continued

(1) Name	(2) Alt Name	(3) RA	(4) DEC	(5) Type	(6) cz	(7) Log Density
UGC 12535	—	23:21:01.6	+08:10:46	4	4214	-1.44
UGC 12544	—	23:21:45.1	+09:04:40	10	2859	-1.40
UGC 12553	—	23:22:13.7	+09:23:03	10	3573	-0.15
UGC 12562	—	23:22:47.5	+11:46:22	8	3836	-0.76
NGC 7643	UGC 12563	23:22:50.4	+11:59:20	2	3878	-0.46
UGC 12561	—	23:22:58.5	+08:59:37	8	3743	-0.43
UGC 12580	—	23:24:33.8	+08:36:58	1	3033	-1.36

Table 2. Additional Galaxy Data

(1) Name	(2) DEF	(3) Γ	(4) Γ^*	(5) M_H	(6) r_{10} (")	(7) $\frac{r_{H\alpha}}{r_{10}}$	(8) r_{eff} (")	(9) $\gamma(0.1)$	(10) Δ	(11) $\Gamma_{H\alpha}$
Non-Pegasus Galaxies										
NGC 41	0.01	-1.84	-1.72	-23.62	33.	0.82	10.	-1.97	-0.13	-1.96
UGC 144	0.96	-3.10	-3.08	-22.67	31.	0.43	12.	-2.39	0.71	-2.75
UGC 164	0.99	-2.24	-2.18	-23.05	45.	0.80	26.	-1.28 ^b	0.96	-2.11
NGC 352	-0.05	-2.49	-2.25	-24.83	76.	0.79	26.	-2.04	0.45	-2.66
UGC 1026	0.40	-2.83	-3.13	-19.63 ^a	27.	—	14.	—	—	—
IC 1721	0.30	-1.85	-1.83	-22.72	32.	0.74	12.	-2.06	-0.21	-1.82
CGCG 059-019	0.78	-2.62	-2.63	-22.41 ^a	29.	0.66	13.	—	—	-2.72
NGC 5417	0.65	-3.88	-3.66	-24.63	52.	0.28	12.	-2.68	1.20	-3.29
IC 1132	-0.18	-1.95	-1.88	-23.14	39.	0.83	17.	-1.95	0.00	-2.00
NGC 5990	0.21	-2.14	-2.00	-23.83 ^a	53.	0.51	11.	-2.45	-0.31	-2.42
IC 1205	-0.42	-1.82	-1.85	-22.20	22.	0.69	8.	-2.02	-0.20	-1.88
UGC 11524	-0.52	-1.74	-1.61	-23.73	38.	1.08	18.	-2.45	-0.71	-1.57
CGCG 373-007	0.67	-3.05	-3.15	-21.54	29.	0.14	12.	-2.35	0.70	—
NGC 7074	0.52	-1.92	-1.92	-22.52	35.	0.53	12.	-1.43 ^b	0.49	-1.99
NGC 7081	-0.28	-1.79	-1.82	-22.21	39.	0.69	10.	-1.86	-0.07	-1.71
CGCG 402-018	0.11	-2.00	-2.07	-21.86 ^a	29.	0.68	14.	-2.19	-0.19	-2.05
UGC 11848	-0.05	-2.01	-2.24	-20.31 ^a	30.	1.00	15.	-2.13	-0.12	-1.87
UGC 12479	-0.41	-2.22	-2.23	-22.38	36.	0.56	10.	-2.01	0.21	-2.26
Pegasus I Cluster Galaxies										
UGC 12304	0.38	-2.31	-2.28	-22.81	—	—	—	—	—	—
UGC 12361	0.01	-2.15	-2.31	-20.98 ^a	—	—	—	—	—	—
UGC 12370	-0.04	-2.26	-2.34	-21.70	41.	0.62	14.	-1.85	0.40	-2.10
IC 1474	-0.05	-1.94	-1.93	-22.63	34.	0.93	14.	-2.33	-0.39	-2.07
NGC 7518	0.27	-2.23	-2.16	-23.21	43.	0.61	22.	-1.49 ^b	0.74	-2.18
NGC 7529	-0.08	-1.99	-2.03	-22.16	29.	0.72	11.	—	—	-2.19
NGC 7537	-0.31	-1.76	-1.77	-22.36	57.	1.00	14.	-1.93	-0.17	-1.78
NGC 7541	-0.10	-1.92	-1.76	-24.06 ^a	—	—	—	—	—	—
UGC 12451	0.24	-1.98	-2.30	-19.43	50.	0.88	36.	-2.19	-0.21	—
NGC 7563	1.82	-5.40	-5.22	-24.27	53.	0.00	10.	—	—	—
UGC 12467	0.32	-2.14	-2.18	-22.08 ^a	59.	0.64	26.	-2.20	-0.06	-2.13
CGCG 406-042	0.41	-2.38	-2.59	-20.51	29.	0.77	16.	-2.85	-0.47	-2.17
NGC 7580	-0.29	-1.76	-1.74	-22.70	26.	0.64	8.	-1.23	0.53	-2.15
NGC 7593	0.07	-1.99	-1.98	-22.64	34.	0.61	14.	-1.79	0.20	-1.96
NGC 7591	-0.25	-1.96	-1.77	-24.32	62.	1.04	14.	-1.52	0.44	-1.73
UGC 12494	0.06	-1.90	-2.01	-21.44	43.	0.88	20.	-1.67	0.23	-1.85
UGC 12497	-0.04	-2.22	-2.25	-22.19 ^a	42.	0.46	20.	-1.84	0.38	-2.69
IC 5309	0.29	-2.00	-1.95	-22.95	56.	0.54	19.	-1.83	0.17	-2.07
NGC 7608	0.48	-2.07	-2.05	-22.56	47.	0.87	20.	-1.69 ^b	0.38	-2.04
NGC 7610	-0.15	-1.30	-1.32	-22.29	55.	1.00	22.	-1.64	-0.34	-1.39

Table 2—Continued

(1)	(2)	(3)	(4)	(5)	(6)	(7)	(8)	(9)	(10)	(11)
Name	DEF	Γ	Γ^*	M_H	r_{10} (")	$\frac{r_{H\alpha}}{r_{10}}$	r_{eff} (")	$\gamma(0.1)$	Δ	$\Gamma_{H\alpha}$
NGC 7615	0.85	-2.52	-2.53	-22.45	29.	0.79	11.	—	—	-2.46
UGC 12522	0.19	-2.24	-2.43	-20.69	35.	0.30	20.	-2.39	-0.15	-2.28
UGC 12535	0.51	-2.11	-2.15	-22.07	40.	0.68	16.	-1.64 ^b	0.47	-2.13
UGC 12544	-0.06	-2.11	-2.27	-20.99 ^a	38.	0.65	20.	—	—	-2.25
UGC 12553	0.16	-2.80	-2.80	-20.99 ^a	26.	—	15.	—	—	—
UGC 12562	0.16	-2.05	-2.41	-19.03	37.	0.67	15.	-2.34	-0.29	-2.05
NGC 7643	0.65	-2.37	-2.27	-23.44	46.	0.57	20.	-1.63 ^b	0.74	-2.33
UGC 12561	0.19	-2.98	-3.07	-21.60 ^a	43.	0.12	20.	-2.32	0.66	—
UGC 12580	1.11	-3.69	-3.74	-22.05	37.	0.05	9.	-2.39	1.36	—

^aNo H band data is available from Hyperleda; M_H was determined from total absolute B magnitude and an assumed $B - H$ color of -2.52.

^bGalaxies with high DEF and high central SSFR ($\gamma(0.1)$)

REFERENCES

- Abadi, M. G., Moore, B., & Bower, R. G. 1999, MNRAS, 308, 947
- Boselli, A., & Gavazzi, G. 2006, PASP, 118, 517
- Bothun, G. D., & Dressler, A. 1986, ApJ, 301, 57
- Bravo-Alfaro, H., Cayatte, V., van Gorkom, J. H., & Balkowski, C. 2001, A&A, 379, 347
- Butcher, H., & Oemler, A., Jr. 1978, ApJ, 219, 18
- Butcher, H., & Oemler, A., Jr. 1984, ApJ, 285, 426
- Byrd, G., & Valtonen, M. 1990, ApJ, 350, 89
- Caldwell, C., Rose, J. A., Sharples, R. M., Ellis, R. S., & Bower, R. G. 1993, AJ, 106, 473
- Caldwell, C., Rose, J. A., Franx, M., & Leonardi, A. J. 1996, AJ, 111, 78
- Caldwell, N., & Rose, J. A. 1997, AJ, 113, 492
- Caldwell, N., Rose, J. A., & Dendy, K. 1999, AJ, 117, 140
- Cayatte, V., Kotanyi, C., Balkowski, C., & van Gorkom, J. H. 1994, AJ, 107, 1003
- Chung, A., van Gorkom, J. H., Kenney, J. D. P., & Vollmer, B. 2007, ApJ, 659, L115
- Clemens, J. C., Crain, J. A., & Anderson, R. 2004, SPIE, 5492, 331
- Cortes, J. R., Kenney, J. D. P., & Hardy, E. 2008, ApJ, 683, 78
- Courteau, S. 1996, ApJS, 103, 363
- Cowie, L. L., & Songaila, A. 1977, Nature, 266, 501
- Crowl, H. H., & Kenney, J. D. P. 2006, ApJ, 649, L75
- Davis, D. S., Keel, W. C., Mulchaey, J. S., & Henning, P. A. 1997, AJ, 114, 2
- Dressler, A. 1980, ApJ, 236, 351
- Dressler, A., & Gunn, J. E. 1983, ApJ, 270, 7
- Dressler, A., Smail, I., Poggianti, B. M., Butcher, H., Couch, W. J., Ellis, R. S., Oemler, A. Jr. 1999, ApJ, 122, 51

- Falco, E. E., Kurtz, M. J., Geller, M. J., Huchra, J. P., Peters, J., Berlind, P., Mink, D. J., Tokarz, S. P., & Elwell, B. 1999, *PASP*, 111, 438
- Focardi, P., & Kelm, B. 2002, *A&A*, 391, 35
- Fumagalli, M., & Gavazzi, G. 2008, *A&A*, 490, 571
- Gavazzi, G. 1987, *ApJ*, 320, 96
- Gavazzi, G., Contursi, A., Carrasco, L., Boselli, A., Kennicutt, R., Scodreggio, M., Jaffe, W. 1995, *A&A*, 304, 325
- Gavazzi, G., O’Neil, K., Boselli, A., & van Driel, W. 2006, *A&A*, 449, 929
- Giovanelli, R., & Haynes, M. P. 1985, *ApJ*, 292, 404
- Gomez, P. L. et al. 2003, *ApJ*, 584, 210
- Goto, T., Yamauchi, C., Fujita, Y., Okamura, S., Sekiguchi, M., Smail, I., Bernardi, M., & Gomez, P. L. 2003, *MNRAS*, 346, 601
- Gunn, J. E., & Gott, J. R. 1972, *ApJ*, 176, 1
- Haynes, M. P., & Giovanelli, R. 1986, *ApJ*, 306, L55
- Hester, J. A. 2006, *ApJ*, 647, 910
- Kapferer, W., Kronberger, T., Ferrari, C., Riser, T., & Schindler, S. 2008, *MNRAS*, 389, 1405
- Kantharia, N. G., Ananthakrishnan, S., Nityananda, R., & Hota, A. 2005, *A&A*, 435, 483
- Kawata, D., & Mulchaey, J. S. 2008, *ApJ*, 672, 103
- Kenney, J. D. P., & Koopmann, R. A., Rubin, V. C., & Young, J. S. 1996, *AJ*, 111, 152
- Kenney, J. D. P., & Koopmann, R. A. 1999, *AJ*, 117, 181
- Kenney, J. D. P., van Gorkom, J. H., Vollmer, B. 2004, *AJ*, 127, 3361
- Koopmann, R. A., & Kenney, J. D. P. 1998, *ApJ*, 497, L75
- Koopmann, R. A., & Kenney, J. D. P. 2004, *ApJ*, 613, 851
- Koopmann, R. A., & Kenney, J. D. P. 2004, *ApJ*, 613, 866

- Kronberger, T., Kapferer, W., Ferrari, C., Unterguggenberger, S., & Schindler, S. 2008a, *A&A*, 481, 337
- Kronberger, T., Kapferer, W., Unterguggenberger, S., Schindler, S., & Ziegler, B. L. 2008b, *A&A*, 483, 783
- Landolt, A. U. 1992, *AJ*, 104, 372
- Larson, R. B., Tinsley, B. M., & Caldwell, C. N. 1980, *ApJ*, 237, 692
- Lavery, R. J., & Henry, J. P. 1988, *ApJ*, 330, 596
- Levy, L., Rose, J. A., van Gorkom, J. H., & Chaboyer, B. 2007, *AJ*, 133, 1104
- Marzke, R.O., Huchra, J.P., & Geller M.J. 1994, *ApJ*, 428, 43
- Mihos, J. C., & Hernquist, L. 1994, *ApJ*, 425, L13
- Mihos, J. C., & Hernquist, L. 1996, *ApJ*, 464, 641
- Moore, B., Katz, N., Lake, G., Dressler, A., & Oemler, A. 1996, *Nature*, 379, 613
- Moore, B., Lake, G., & Katz, N. 1998, *ApJ*, 495, 139
- Moss, C., & Whittle, M. 1993, *ApJ*, 407, L17
- Moss, C., & Whittle, M. 2000, *MNRAS*, 317, 667
- Moss, C., & Whittle, M. 2005, *MNRAS*, 357, 1337
- Mulchaey, J. S., Davis, D. S., Mushotzky, R. F., & Burstein, D. 1993, *ApJ*, 404, L9
- Nulsen, P. E. J. 1982, *MNRAS*, 198, 1007
- Oemler, A. 1974, *ApJ*, 194, 1
- Omar, A., & Dwarakanath, K. S. 2005, *J. Astrophys. Astr.*, 26, 71
- Rasmussen, J., Ponman, T. J., & Mulchaey, J. S. 2006, *MNRAS*, 370, 453
- Roediger, E., & Hensler, G. 2005, *A&A*, 433, 875
- Rose, J. A., Gaba, A. E., Caldwell, N. & Chaboyer, B. 2001, *AJ*, 121, 793
- Sanchis, T., Mamon, G. A., Salvador-Sole, E., & Solanes, J. M. 2004, *A&A*, 418, 393
- Schechter, P. 1976, *ApJ*, 203, 297

- Schulz, S., & Struck, C. 2001, MNRAS, 328, 185
- Schwarz, H. E., Ashe, M. C., Boccas, M., Bonati, M., Delgado, F., Gavez, R., Martinez, M., Schurter, P., Schmidt, R., Tighe, R., Walker, A. R. 2004, SPIE, 5492, 564
- Sengupta, C. & Balasubramanyam, R. 2006, MNRAS, 369, 360
- Sengupta, C., Balasubramanyam, R., & Dwarakanath, K. S. 2007, MNRAS, 378, 137
- Solanes, J. M., Giovanelli, R., & Haynes, M. P. 1996, ApJ, 461, 609
- Solanes, J. M., Manrique, A., Garcia-Gomez, C., Gonzales-Casado, G., Giovanelli, R., & Haynes, M. P. 2001, ApJ, 548, 97
- Solanes, J. M., Sanchis, T., Salvador-Sole, E., Giovanelli, R., & Haynes, M. P. 2002, AJ, 124, 2440
- Springob, C. M., Haynes, M. P., Giovanelli, R., & Kent, B. R. 2005a, ApJS, 160, 149
- Springob, C. M., Haynes, M. P., & Giovanelli, R. 2005b, ApJ, 621, 215
- Struck, C., & Brown, J. R. 2004, in IAUS#217, Recycling Intergalactic and Interstellar Matter, ed. P.-A. Duc, J. Braine, & E. Brinks (San Francisco: Astron. Soc. Pac.), p. 466
- Thomas, C. F., Moss, C., James, P. A., Bennett, S. M., Aragon-Salamanca, A., & Whittle, M. 2008, A&A, 486, 755
- Toomre, A., & Toomre, J. 1972, ApJ, 178, 623
- Tosa, M. 1994, ApJ, 426, L81
- van Dokkum, P. G., Franx, M., Fabricant, D., Illingworth, G. D., & Kelson, D. D. 2000, ApJ, 541, 95
- van Gorkom, J. H. 2004, in Carnegie Observatory Astrophysics Series, Vol 3: Clusters of Galaxies, Probes of Cosmology and Galaxy Evolution, ed. J.S. Mulchaey, A. Dressler, and A. Oemler (Cambridge: Cambridge University Press), p306
- Verheijen, M. A. W. 2004, in Outskirts of Galaxy Clusters: intense Life in the Suburbs, ed. A. Diaferio (IAU Colloquium #195), p394
- Vigroux, L., Boulade, O., & Rose, J. A. 1989, AJ, 98, 2044
- Vollmer, B., Cayatte, V., Balkowski, C., & Duschl, W. J. 2001, ApJ, 561, 708

Vollmer, B., Beck, R., Kenney, J. D. P., & van Gorkom, J. H. 2004, *AJ*, 127, 3375

Vollmer, B., Soida, M., Otmianowska-Mazur, K., Kenney, J. D. P., van Gorkom, J. H., & Beck, R. 2006, *A&A*, 453, 883

Yoshida, M., Yagi, M., Komiyama, Y., Furusawa, H., Kashikawa, N., Koyama, Y., Yamanoi, H., Hattori, T., & Okamura, S. 2008, *ApJ*, 688, 918